Turbulent Mixing with Scale Breaking Phenomena

A Dissertation Presented

by

Xinfeng Liu

to

The Graduate School in Partial Fulfillment of the Requirements for the

Degree of

Doctor of Philosophy

in

Applied Mathematics and Statistics

Stony Brook University

May 2006

Stony Brook University

The Graduate School

Xinfeng Liu

We, the dissertation committee for the above candidate for the Doctor of Philosophy degree, hereby recommend acceptance of this dissertation.

James Glimm
Advisor
Department of Applied Mathematics and Statistics

Xiaolin Li
Chairman
Department of Applied Mathematics and Statistics

Yongmin Zhang
Member
Department of Applied Mathematics and Statistics

Roman Samulyak
Outside Member
Brookhaven National Laboratory
Center for Data Intensive Computing

This dissertation is accepted by the Graduate School.

Graduate School

Abstract of the Dissertation

Turbulent Mixing with Scale Breaking Phenomena

by

Xinfeng Liu

Doctor of Philosophy

in

Applied Mathematics and Statistics

Stony Brook University

2006

Advisor: James Glimm

We study the Rayleigh-Taylor (RT) instability in both the moderately compressible and weakly compressible regimes. Rayleigh-Taylor mixing is an acceleration driven instability of a layer separating two fluids of distinct densities. For the two dimensional single mode case, we find that the dimensionless terminal velocities (and associated Froude numbers) are nearly constant over most of this region of parameter space, as the thermodynamic parameters describing the equation of state are varied. The phenomenological drag coefficient which occurs in the single mode buoyancy-drag equation is directly related to the terminal velocities and has a similar behavior. Pressure differences and interface shape, however, display significant dependence on the EOS parameters even for the weakly compressible flows. For three dimensional multimode mixing, we expect that density stratification rather than drag will provide the leading compressibility effect. We develop an analytical model

to account for density stratification effects in multimode self-similar mixing. Our theory is consistent with and extends numerically based conclusions developed earlier which also identify density stratification as the dominant compressibility effect for multimode three dimensional mixing.

New simulations with Locally Grid Based Front Tracking Method compare Rayleigh-Taylor mixing rates for ideal fluids and for real fluids with experimental values for surface tension or mass diffusion. The simulated real fluid mixing rates agree with those measured experimentally. Comparison to theoretical predictions relating the mixing rate, the bubble width and the bubble height fluctuations based on bubble merger models shows similar agreement with experiment. The ideal fluid mixing rate is some 50% larger, providing an example of the sensitivity of the mixing rate to physical scale breaking interfacial phenomena; we also observe sensitivity to numerical scale breaking artifacts.

Key Words: Rayleigh-Taylor instability, front tracking method, surface tension, mass diffusion.

To my parents, my loving wife and son

Table of Contents

List of Figures

List of Tables

Acknowledgements

It is a great pleasure to thank my thesis advisor, Professor James Glimm, for suggesting and introducing this important and exciting topic and for his advice, support and guidance toward my Ph.D. degree. I am deeply impressed by his keen insight and scientific manner doing research, which will benefit me a lot in my future study. His scientific vigor and dedication makes him a lifetime role model for me.

I would like to express my profound gratitude to Professor Xiaolin Li. It is he who first introduced me into FronTier code. From him, I have learned many scientific and mathematical skills. Without his help, I can not become a professional programmer and debugger so quickly.

I would like to thank Professor Roman Samulyak and Yongmin Zhang, for being my committee members and for helpful discussions.

I would like to thank all of my friends, for their friendship and encouragement, and for sharing with me many interesting and inspiring ideas. In particular, I want to mention Zhiliang Xu, Erwin George, Yan Yu, Wurigen Bo, Jian Du, Yuanhua Li, and Tianshi Lu.

I would like to thank my parents, my wife and my son, for their unconditional support and love. My dissertation is dedicated to them.

Chapter 1

Introduction

Chaotic mixing is a common and important phenomena in basic science and in engineering applications. Small disturbances in a multifluid system produce buoyancy and shear driven instabilities at an interface between distinct fluids [9]. These instabilities grow and develop into turbulent mixing zones consisting of bubbles of light fluid and spikes of heavy fluid, each penetrating into the opposite fluid. The evolution and structure of these mixing zones have been studied for several decades. See for example [32, 40, 47, 51]. The location of the two edges of the mixing zone plays a distinguished role, as the simplest and primary descriptor of the mixing process. The study of mixing processes is not only of theoretical interest. It also plays an important role in the study of inertial confinement fusion and late time supernova evolution.

The Rayleigh-Taylor (RT) instability occurs when a fluid of low density, ρ_l, accelerates a fluid of heavy density, ρ_h. This, and related mixing problems have attracted the attention of leading physicists and mathematicians, beyond Rayleigh and Taylor, and including Kelvin, Wheeler, Garabedian, Birkhoff, and Chandrasekhar among others.

The RT mixing rate is the dimensionless coefficient α in the equation

$$h = \alpha A g t^2 \tag{1.1}$$

for the height h of the bubbles, *i.e.,* the interpenetration distance h of the light fluid into the heavy fluid. Here $A = (\rho_h - \rho_l)/(\rho_h + \rho_l)$ is the Atwood number and t is the time. Acceptable experimental values for α are $\alpha = 0.063 \pm 0.013$ [48]. See [47] for background information. With no surface tension or mass diffusion in the simulation, we find an increased mixing rate. For ideal fluid flow, we find the value $\alpha = 0.09$. However, using physical values of surface tension (for immiscible fluids from [44, 48]), we find $\alpha = 0.067$. Also $\alpha = 0.069$ for miscible fluids with physical values for mass diffusion [6]. The h *vs.* Agt^2 plot has a straight line shape after an initial transient, and we here report the slope obtained by joining the initial to the final point. Defining α in terms of the slope after the initial transient gives a slightly lower value 0.060 for the immiscible fluids. (Here we interpolate between adjacent simulations.)

The dynamical equations governing fluid flow are based on the principles of conservation of mass, momentum, and energy. To complete the system, an equation of state (EOS) relating the state variables is necessary. The equations are

$$\begin{aligned} &\frac{\partial \rho}{\partial t} + \nabla \cdot (\rho v) = 0 \ , \\ &\frac{\partial (\rho v)}{\partial t} + \nabla \cdot \rho v v + \nabla P = \rho g + \nabla \cdot \tau_{ij} \ , \\ &\frac{\partial (\rho E)}{\partial t} + \nabla \cdot ((\rho E + P) v) = \rho v \cdot g + \frac{\partial Q}{\partial t} - \nabla \cdot q + \nabla \cdot (\tau_{ij} v) \ . \end{aligned} \tag{1.2}$$

Here ρ is density, $\nabla = \left\langle \frac{\partial}{\partial x_1}, \frac{\partial}{\partial x_2}, \frac{\partial}{\partial x_3} \right\rangle$, v is the velocity vector, P is the pressure, g is gravity, $\tau_{ij} = \left[\mu \left(\frac{\partial v_i}{\partial x_j} + \frac{\partial v_j}{\partial x_i} \right) - \frac{2}{3} \delta_{ij} \mu \frac{\partial v_k}{\partial x_k} \right]$ is the viscous stress tensor with dynamic viscosity μ, E is the total specific energy, Q is the external heat added per unit volume, and q is the heat flux vector.

The system of equations above is known as the Naiver-Stokes Equations, and the viscous stress tensor τ discusses the internal friction (viscosity) of the fluid. This internal friction

results in a resistance to flow. Although every fluid has some amount of internal friction, many fluids can be modeled quite accurately while neglecting the viscosity. Such fluids are called ideal.

For ideal fluids the system reduces to

$$\begin{aligned} &\frac{\partial \rho}{\partial t} + \nabla \cdot (\rho v) = 0 \ , \\ &\frac{\partial \rho v}{\partial t} + \nabla \cdot (\rho v v) = \nabla P + \rho g \ , \\ &\frac{\partial (\rho E)}{\partial t} + \nabla \cdot ((\rho E + P) v) = \rho v \cdot g \ . \end{aligned} \tag{1.3}$$

The Euler equations in three dimensions are used to model the Rayleigh-Taylor instability.

Front tracking provides sharp resolution of wave fronts through the active tracking of interfaces between distinct materials. It is a numerical method that represents interfaces explicitly as a lower dimensional mesh moving through a volume filling grid. The time step of the front tracking code *FronTier* consists of two parts, the finite difference interior solver for the states defined on the volume filling rectangular grid and front propagation for the front position and states defined on each side of the front, see [12, 24, 25, 27, 28, 33]. This propagation of the front points and front state variables distinguishes front tracking from other numerical methods. We use a directionally split method, which breaks the front propagation into normal and tangential steps. For the normal front propagation, we project Eq. (1.3) to the front normal direction to yield the one dimensional system

$$\begin{aligned} &\frac{\partial \rho}{\partial t} + \frac{\partial \rho v_N}{\partial N} = 0, \\ &\frac{\partial \rho v_N}{\partial t} + \frac{\partial (\rho v_N^2 + P)}{\partial N} = \rho g_N, \\ &\frac{\partial \rho v_T}{\partial t} + \frac{\partial \rho v_N v_T}{\partial N} = 0, \\ &\frac{\partial \rho E}{\partial t} + \frac{\partial \left(\rho E v_N + P v_N \right)}{\partial N} = \rho g_N v_N \ , \end{aligned} \tag{1.4}$$

where $\frac{\partial}{\partial N}$ is the directional derivative in the normal direction $\vec{N}$, $v_N = \mathbf{v} \cdot \vec{N}$, $g_N = g \cdot \vec{N}$, and $v_T = \mathbf{v} - v_N \vec{N}$ is the tangential velocity component.

The tangential projection of Eq. (1.3) is given by

$$\begin{aligned} &\frac{\partial \rho}{\partial t} + \nabla_T \cdot (\rho v_T) = 0 \ , \\ &\frac{\partial \rho v}{\partial t} + \nabla_T \cdot (\rho v v) + \nabla_T P = \rho g_T \ , \\ &\frac{\partial (\rho E)}{\partial t} + \nabla_T \cdot ((\rho E + P) v) = \rho v_T \cdot g_T \ . \end{aligned} \tag{1.5}$$

here ∇_T is the spatial gradient in the tangent plane.

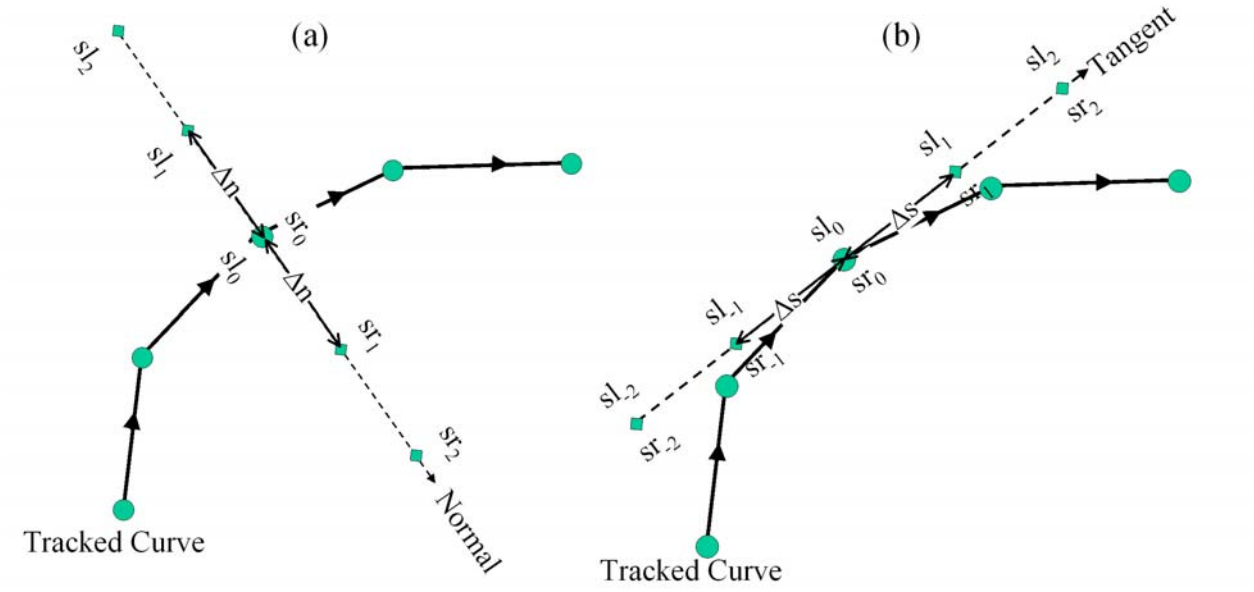

Figure 1.1: A schematic showing the normal propagation stencil of states used in propagating a front point. For simplicity the diagram is shown for two spatial dimensions.

The normal propagation consists of two basic steps, prediction using Riemann problem solutions, and correction to account for flow gradients on either side of the front and to include body or geometry source terms. At material interfaces surface tension may also be

included by modifying the Riemann problem solution to allow a pressure jump proportional to the mean curvature at the point being propagated. For the tangential sweep, since it reduces to a regular finite difference stencil, any of a variety of standard solvers may be used to compute the solution. In contrast to the normal sweep, no additional motion is accounted for in the tangential direction.

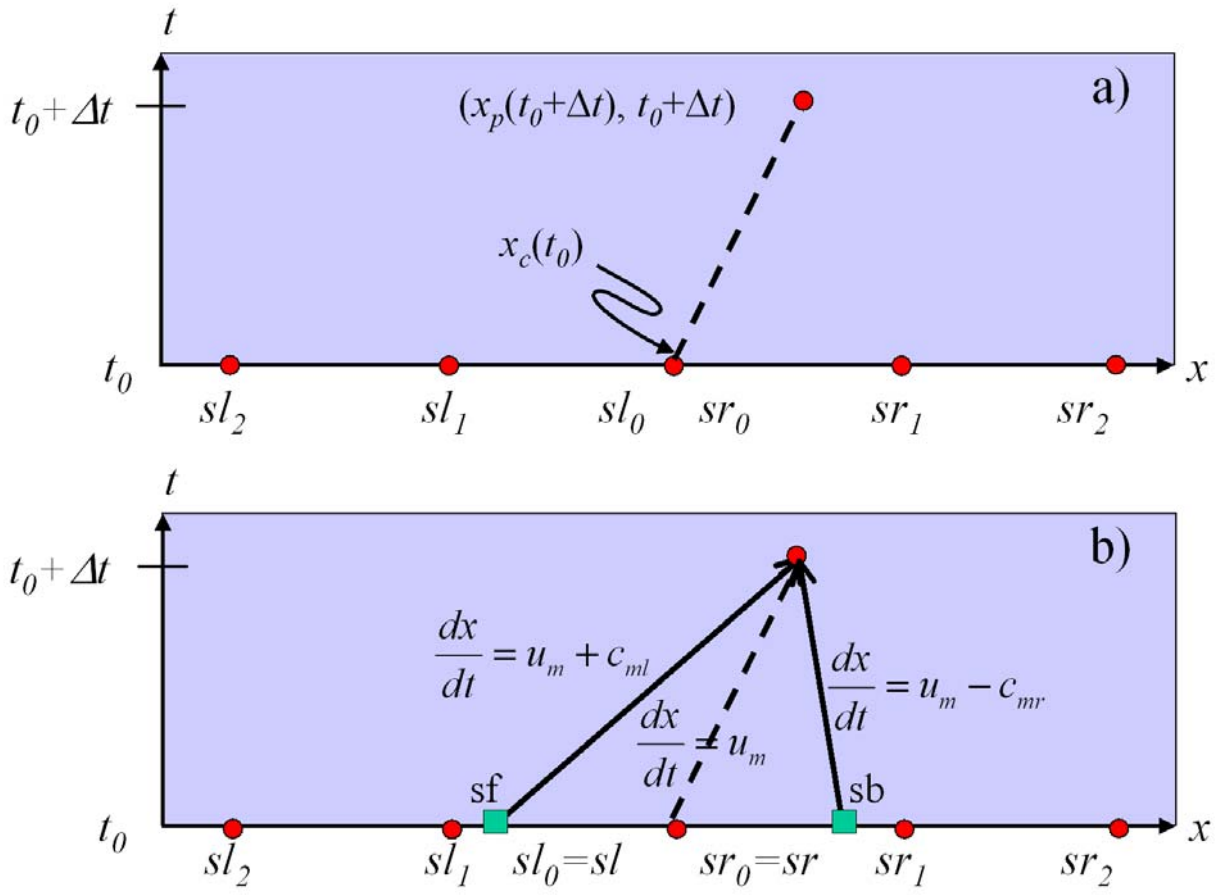

Figure 1.2: The normal propagation project the flow state onto a line normal to the interface point. A one dimensional Cauchy problem is solved to compute an updated front position and state.

Chapter 1 gives a brief review of the Rayleigh-Taylor mixing rates.

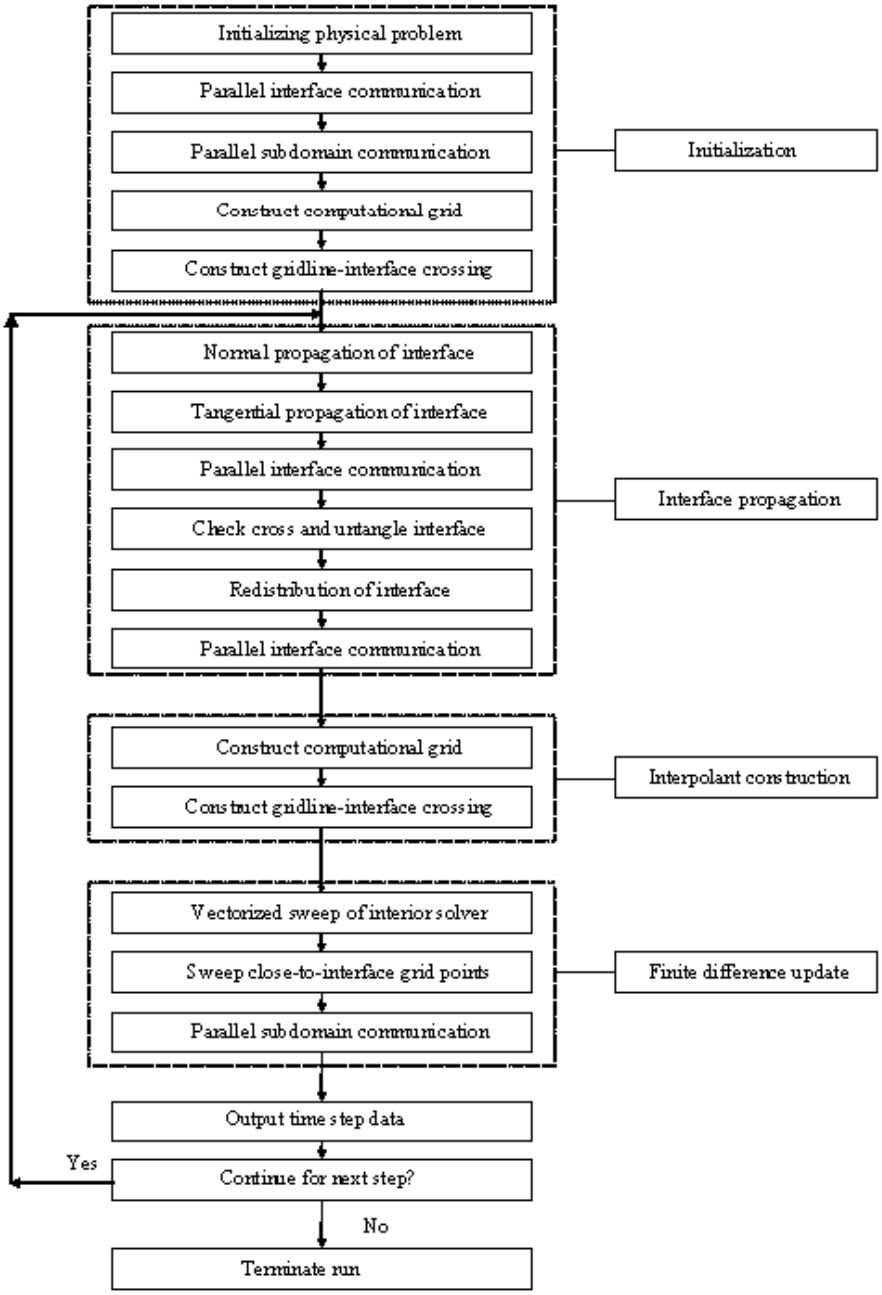

Figure 1.3: Flow control for the front tracking computation. With the exception of the i/o and the sweep and communication of interior points, all solution steps indicated here are specific to the front tracking algorithm itself.

Chapter 2, Chapter 3 and Chapter 4 are the core of my work. In Chapter 2, the single mode RT simulations at terminal velocity are not affected by density stratification, but due to the much longer time and perturbation heights needed to achieve self-similarity for multi mode RT flows, density stratification is a leading compressibility effect for multi mode flows. The stratification is measured by a time and space dependent Atwood number. In §2.2, we propose a simple physics model for this stratification. The ambient fluids are assumed (at $t = 0$) to be isothermal. The penetrating fluids are assumed to have a single pressure at the bubble and spike tips and to change isentropically as they are displayed from their $t = 0$ isothermal state. Then formulas (2.8) and (2.9) yield a model for $A = A_b(z, t)$ and $A = A_s(z, t)$ at the bubble and spike tips. These formulas are compared to direct simulation data. On the basis of §2.1 results, we assume that the drag coefficient is only weakly sensitive to compressibility. On the basis of these two assumptions, we examine the solutions of the buoyancy drag equation to predict compressibility effects on multimode RT mixing rates. We find density stratification as the leading compressibility effect. These predictions are compared to Direct Numerical Simulations.

In Chapter 3 and Chapter 4, we compare new simulations of Rayleigh-Taylor mixing rates for ideal fluids and for real fluids with experimental values for surface tension or mass diffusion, based on an improved Front Tracking code [18]. The primary improvement is to use local grid based tracking, which greatly minimizes the interpolative smoothing of the interface during time steps which display interface bifurcation. The grid based algorithm previously used handles bifurcations robustly, but with excess interpolation, and now the grid based reconstruction is applied only in local regions where needed and not globally as before. Detailed comparison [18] documents the advantage of the new algorithm relative to the old, in reducing excess smoothing of the interface, and its advantages relative to other interface algorithms such as level sets [38] and volume of fluids [45] algorithms. Untracked simulations are by a total variation diminishing (TVD) algorithm.

Simulated mixing rates of Rayleigh-Taylor instability for miscible fluids with physical mass diffusion are shown to agree with experiment; for immiscible fluids with physical values of surface tension the numerical data lies in the center of the experimental values. The simulations are based on an improved front tracking algorithm to control numerical surface tension and on improved physical modeling to allow physical values of mass diffusion or surface tension. Compressibility, after correction for variable density effects, has also been shown to have a strong influence on mixing rates. In summary, we find significant dependence of the mixing rates on scale breaking phenomena. We introduce tools to analyze the bubble merger process and confirm that bubble interactions, as in a bubble merger model, drive the mixing growth rate.

The conclusion is presented in Chapter 5.

Chapter 2

Compressibility Effects on Rayleigh-Taylor Mixing Rates

In this chapter, we examine first the well studied case of a single mode RT instability, *i.e.,* a periodic array of identical modes, consisting of bubbles of light fluid rising into the heavy fluid and spikes falling into light fluid, under gravitational acceleration of an initially unstable (heavy over light) configuration. The modes grow initially at an exponential rate but eventually saturate, and achieve a terminal velocity

$$|V_{b,s}^{\infty}| = C_{b,s}\sqrt{Ag\lambda} \quad , \tag{2.1}$$

with an Atwood number $A = (\rho_2 - \rho_1)/(\rho_2 + \rho_1)$ expressing the contrast in fluid densities between $\rho_1 = \rho_{\text{light}}$ and $\rho_2 = \rho_{\text{heavy}}$, $g = g(t)$ the gravitational acceleration, and λ the width of the periodic channel. Here the subscript "b" denotes bubble (light fluid penetrating into heavy fluid) and "s" denotes spike. $C_{b,s}^2$ is called the Froude number and it has been studied theoretically [8, 19, 37] and numerically [53]. For bubbles, it has the values $C_b = 0.23$ in two dimensions and $C_b = 0.34$ in three dimensions for $A = 1$ according to analytic theories [8, 19, 37] confirmed by experiment and two dimensional simulations [42]. Alternate

forms of (2.1) have been proposed [43] with A replaced by $2A/(A \pm 1)$ when $A < 1$,

$$|V_{b,s}^{\infty}| = C'_{b,s}\sqrt{\frac{2Ag\lambda}{A \pm 1}}\ , \quad C'_{b,s} = C_{b,s}\sqrt{\frac{A \pm 1}{2}}\ \ . \tag{2.2}$$

A more fundamental finite A theory for $C_{b,s}$ with a more complicated A dependence has been presented recently [3, 4]. A correction to this basic picture was identified as a late time oscillation in $V_{b,s}$ about some mean value [29]. Moreover, the $A = 1$ Froude number in 3D depends on the planar symmetry group of the periodic bubbles [1, 2] and this effect should hold for$A < 1$ also.

We discuss compressibility effects in RT mixing. We show in §2.1 that bubble and spike terminal velocities, *i.e.,* the $C_{b,s}$ and the related single mode drag coefficients introduced below are relatively insensitive to the compressible equation of state (EOS) parameters over the range of parameters we examine, for moderately compressible and nearly incompressible flows. However, a detailed examination of the interface shapes and of the pressure differences between the heavy and light fluids, averaged at a common height, shows a strong dependence on EOS parameters. Thus convergence to a unique incompressible limit is not achieved within the very slightly compressible flows considered here.

We measure compressibility through the pseudo Mach number

$$M_i = \frac{\sqrt{g\lambda}}{c_i}\ , \tag{2.3}$$

where c_i is the sound speed in fluid i. In view of (2.1),

$$M_i = \frac{1}{C_{b,s}\sqrt{A}} \times \text{ Mach number} \tag{2.4}$$

is approximately five times the Mach number ($|V_{b,s}^{\infty}|/c_i$) of the bubble or spike tip at its terminal velocity for the value of $A = 1/3$ considered here. The dimensionless parameters

governing compressible single mode RT mixing are M_i, A and the EOS.

The complete EOS of a compressible fluid contains an infinite number of parameters. These should become irrelevant in the limit $M_i^2 \to 0$. For simplicity, we consider a simple model for the EOS, the stiffened γ-law gas, defined by the incomplete EOS

$$\rho c^2 = \gamma(p + P_\infty) \ , \tag{2.5}$$

where P_∞ is a constant with the dimension of pressure. The RT instability with this EOS depends on four thermodynamic parameters, γ_1, γ_2, $P_{1\infty}$ and $P_{2\infty}$, as well as the flow parameters A and M_2 (M_1 is determined from M_2 and the thermodynamics). M_i^2 can also be understood as giving a length scale (in units of λ) over which compression induced density changes occur. Hydrostatic equilibrium is defined as a solution of the static momentum equation

$$\frac{dp}{dz} = \rho g \ . \tag{2.6}$$

The dependence of ρ (and thus p) on z can be specified initially by an arbitrary function of z.

Two natural choices for this initial $\rho(z)$ are defined by isothermal or isentropic thermodynamics. Assuming an isothermal initialization and a stiffened γ-law gas, the sound speeds are initially constant in each fluid and the density satisfies

$$\frac{d\rho}{dz} = \frac{\gamma \rho g}{c^2} \ . \tag{2.7}$$

Eq. (2.7) is integrated to yield

$$\rho_i(z) = \rho_i^0 \exp\left[\frac{\gamma_i g(z - z_{\rm int})}{c_i^2}\right] = \rho_i^0 \exp\left[\frac{\gamma_i M_i^2 (z - z_{\rm int})}{\lambda}\right] \ , \tag{2.8}$$

where $z_{\rm int}$ is the initial mean interface position and ρ_i^0 is the density of fluid i at $z = z_{\rm int}$. For a bubble or spike penetrating into an isothermally stratified ambient fluid, we assume a common horizontally averaged pressure in the two fluids as a function of z and isentropic density stratification in the penetrating phase. Using the ambient pressure from (2.7) and (2.8), we derive the formula

$$\rho_i(z) = \rho_i^0 \left\{ \mathcal{T}_i^0 \exp\left[\frac{\gamma_{i'} M_{i'}^2 (z - z_{\rm int})}{\lambda} \right] - \mathcal{T}_i^0 + 1 \right\}^{\frac{1}{\gamma_i}} , \tag{2.9}$$

where

$$\mathcal{T}_i^0 = \frac{\gamma_i M_i^2 \rho_{i'}^0}{\gamma_{i'} M_{i'}^2 \rho_i^0} = \frac{P_0 + P_{i'\infty}}{P_0 + P_{i\infty}} = \frac{1}{\mathcal{T}_{i'}^0} \tag{2.10}$$

is the relative stiffness of two fluids, $p_i = p_{i'} = P_0$ is the single pressure at $z = z_{\rm int}$ and the primed index i' denotes the fluid complementary to fluid i, *i.e.*, $i' = 3 - i$. Notice that $\mathcal{T}_i^0 = 1$ in case $P_{i\infty} = P_{i'\infty}$.

2.1 Single Mode Mixing Rates

Multimode (chaotic) mixing rates are defined as solutions of the the buoyancy drag equation

$$(\rho_i + \kappa_i \rho_{i'}) \frac{d^2 Z_i}{dt^2} = (\rho_i - \rho_{i'}) g - (-1)^i \frac{C_i^d \rho_{i'} V_i^2}{|Z_i|} . \tag{2.11}$$

This equation describes the one dimensional motion of the interfaces of an acceleration driven mixing layer. Here $i = 1$ (bubble) and $i = 2$ (spike) denote the light and heavy fluids, respectively, $V_i \equiv \dot{Z}_i(t) = dZ_i/dt$ and $i' = 3 - i$. ρ_i is the mass density of fluid i, κ_i is an added mass coefficient due to the existence of fluid i', and C_i^d is a phenomenological drag coefficient for the edge of fluid i, which has the functional form [10]

$$C_i^d(A) = \frac{1/\alpha_i - [1 + (-1)^i A] - \kappa_i L_i}{2 L_i} , \tag{2.12}$$

where $L_i = 1 - (-1)^i A$i and α_i is the mixing rate of bubble height ($i = 1$) or spike height ($i = 2$).

We discuss the buoyancy drag equation (2.11) for single mode RT mixing with cylindrical compressible front bubbles and spikes ($\kappa_i \approx 1$). Since $dV_i/dt = 0$ at the terminal velocity, $V_i = V_i^\infty$, we obtain

$$Ag = \frac{L_i}{2} \frac{C_i^{d,s} V_i^2}{|Z_i|} \ , \tag{2.13}$$

where $C_i^{d,s}$ denotes the single mode value of C_i^d. From (2.13), we evaluate the terminal velocity

$$|V_i^\infty| = \sqrt{\frac{2Ag|Z_i|}{L_i C_i^{d,s}}} = \sqrt{Ag\lambda} \times \sqrt{\frac{2}{L_i C_i^{d,s}}} \tag{2.14}$$

by setting $\lambda = |Z_i|$. The identity (2.14) shows the dependence of V_i^∞ on $2A/L_i = 2A/(1 - (-1)^i A)$ which replaces A in an alternate form of (2.1). The comparison of (2.14) with (2.1) gives the Froude number

$$C_{1,2} = \sqrt{\frac{2}{L_i C_i^{d,s}}} \ . \tag{2.15}$$

2.1.1 Zhang's Model

The conventional bubble (spike) velocity development for the single mode RT instability has three different stages: linear, free fall, and terminal velocity regime. Qiang Zhang proposed an ODE model to fit such a velocity profile. There are four parameters to characterize the motion of the spike or bubble: the growth rate β in the linear regime, the renormalized gravity g_R in the free fall regime, the terminal velocity v_∞ in the terminal velocity regime, and the decay rate δ from free fall to terminal velocity. The assumption is that the velocity profile should satisfy the equation

$$\frac{dv}{dt} = \beta v (1 - \frac{v}{v_\infty}) f(v) \ , \tag{2.16}$$

where $f(v)$ is a positive function satisfying $f(0) = 1$ and $f(v_\infty) = \delta/\beta$. Since σ and v_∞ appear in Eq. (2.16) already, there should be two parameters in the function $f(v)$. Assume $f(v)$ has the form

$$f(v) = \frac{1}{1 + \phi_1 v/v_\infty + \phi_2 v^2/{v_\infty}^2} \ , \tag{2.17}$$

where ϕ_1 and ϕ_2 are dimensionless constants. Eq. (2.16) becomes

$$\frac{dv}{dt} = \frac{\beta v(1 - \frac{v}{v_\infty})}{1 + \phi_1 v/v_\infty + \phi_2 v^2/{v_\infty}^2} \ . \tag{2.18}$$

To solve for the parameters ϕ_1 and ϕ_2, the maximum v_f of the acceleration in Eq. (2.18), one needs to satisfy the linear growth rate β, and the terminal velocity decay rate δ/β in Eq. (2.17). From Eq. (2.18), the maximum acceleration v_f satisfies

$$1 - 2\frac{v_f}{v_\infty} - (\phi_1 + \phi_2)\frac{v_f^2}{v_\infty^2} = 0 \ . \tag{2.19}$$

From Eq. (2.19) and the maximum v_f in Eq. (2.16), we have

$$\phi_1 + \phi_2 = v_\infty \frac{v_\infty - 2v_f}{v_f^2} = 0 \ , \tag{2.20}$$

and

$$\frac{\delta}{\beta} = f(v_\infty) = \frac{1}{1 + \phi_1 + \phi_2} \ . \tag{2.21}$$

The renormalized gravity is given by setting v to v_f in Eq. (2.18),

$$g_R = \frac{\beta v_f(1 - v_f/v_\infty)}{1 + \phi_1 v_f/v_\infty + \phi_2 v_f^2/v_\infty^2} \ . \tag{2.22}$$

Thus ϕ_1 and ϕ_2 are obtained through the solution of Eqs. (2.19), (2.20), and (2.21).

$$\phi_1 = \frac{\beta v_\infty}{g_R} - 2(1 + \sqrt{\frac{\beta}{\delta}}) \ , \tag{2.23}$$

and

$$\phi_2 = -\frac{\beta v_\infty}{g_R} - 2(1 + \sqrt{\frac{\beta}{\delta}})^2 \ . \tag{2.24}$$

Eq. (2.18) can be rewritten as

$$\frac{dv}{dt} = \frac{\beta v(1 - \dfrac{v}{v_\infty})}{\dfrac{\beta v}{\delta v_\infty} + (1 - \dfrac{v}{v_\infty}) + \left[\dfrac{\beta v_\infty}{g_R} - (1 + \sqrt{\dfrac{\beta}{\delta}})^2\right] \dfrac{v}{v_\infty}(1 - \dfrac{v}{v_\infty})} \ . \tag{2.25}$$

The solution for Eq. (2.25) is

$$t - t_0 = \frac{1}{\beta}\ln(\frac{v_t}{v_0}) + \left[\frac{1}{g_R} - (\frac{1}{\sqrt{\beta}} + \frac{1}{\sqrt{\delta}})^2 \frac{1}{v_\infty}\right](v_t - v_0) - \frac{1}{\delta}\ln(\frac{v_\infty - v_t}{v_\infty - v_0}) \ , \tag{2.26}$$

and the solution for the spike or bubble position is

$$\begin{aligned} z - z_0 = (\frac{1}{\beta} - \frac{1}{\delta})(v_t - v_0) + &\left[\frac{1}{g_R} - (\frac{1}{\sqrt{\beta}} - \frac{1}{\sqrt{\delta}})^2 \frac{1}{v_\infty}\right] \frac{v_t^2 - v_0^2}{2} \\ &- \frac{v_\infty}{\delta}\ln(\frac{v_\infty - v_t}{v_\infty - v_0}) \ . \end{aligned} \tag{2.27}$$

For an incompressible one fluid system ($A = 1, \ M^2 = 0$) with wave length λ, the bubble terminal velocity is given by

$$v_\infty^{\text{bubble}}(A = 1, M^2 = 0) = 0.23(\lambda g)^{1/2} \ . \tag{2.28}$$

By using the front tracking method and numerical data fitting, Zhang proposed the following

2D single mode terminal velocity formulas: For the bubble,

$$\frac{v_\infty}{c_h} = c_\infty M^2 A + 0.23 M A^{1/2} \ , \tag{2.29}$$

$$\frac{v_f}{c_h} = c_f M^2 A + c_f M A^{1/2} \ , \tag{2.30}$$

and

$$\frac{g_R}{g} = c_R A^2 + \frac{c_R M A}{1 + c_R M} \ . \tag{2.31}$$

From a dimensional argument, the terminal velocity of the bubble should be proportional to $\sqrt{\lambda g}$, *i.e.,* $v_\infty = c_1 \sqrt{\lambda g}$. Here c_1 is the constant of proportionality and it is a function of the dimensionless parameters A, M, and γ only. From Eq. (2.29) we have

$$c_1 = 0.15 M A + 0.23 A^{1/2} \ . \tag{2.32}$$

Since the same value $\gamma = 1.4$ is used in all simulations, the dependence of c_1 on γ is not explored in Zhang's model.

2.1.2 Compressible EOS Effects

In this section, we show, through an extensive simulation study, that the drag coefficients $\mathcal{C}_i^{s,d}$ and Froude numbers have small sensitivity to EOS parameters in the moderate to weak compressibility regime. In spite of this fact, we show striking EOS dependence even for very weakly compressible flows. The dependence is obvious in the shape of the interface at the time the terminal bubble velocity is achieved, see Fig. 2.1, and in the strong dependence of pressure differences (and pressure drag) on EOS parameters, both for weakly compressible flows.

We performed a systematic study of 2D Rayleigh-Taylor single mode instability simu-

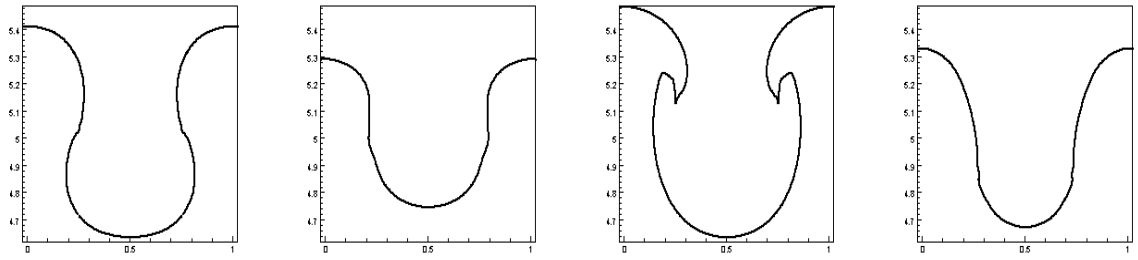

Figure 2.1: The front plots at terminal velocity for the four cases in Table 2.1-2.2. Here $M_2 = 0.05$. Gravity g points upward here, so that the bubble tip is located at the bottom of each figure.

lations, using the front tracking code $FronTier$, with different EOS parameters as in (2.5). In our simulations, we set the Atwood number $A = 1/3$. The initial configuration of the system contains a small amplitude, single sinusoidal mode interface with periodic boundary conditions on the left and right side of the computational domain of width λ. The top and bottom of the computational domain are Neumann boundaries. The initial amplitude of the perturbation is set to 0.015λ. The positions of the interfaces and the states of the system are updated by applying the front tracking method to the full two-dimensional Euler equations. All the numerical results use a 160×1600 grid in a 1×10 computational domain. It is known that the bubble velocity has gradual oscillations associated with gradual shape changes in the bubble and spike, after first reaching a maximum velocity [3], so that the notion of terminal velocity for $A < 1$ is not a precisely defined concept. We take the terminal velocity to be the velocity at the first maximum in these oscillations. We record the first peak as the terminal velocity, after which the velocity is weakly oscillatory as seen in Fig. 2.2. For the pressure differences and drag ratios (bubble or spike), $D^r_{b,s} = \{\text{pressure drag}\}/\{\text{form drag}\}$, there are rapid small oscillations at late time, removed by local time averages in Fig. 2.2.

Table 2.1-2.2 shows that the terminal velocity coefficients $C_{b,s}$ are nearly independent

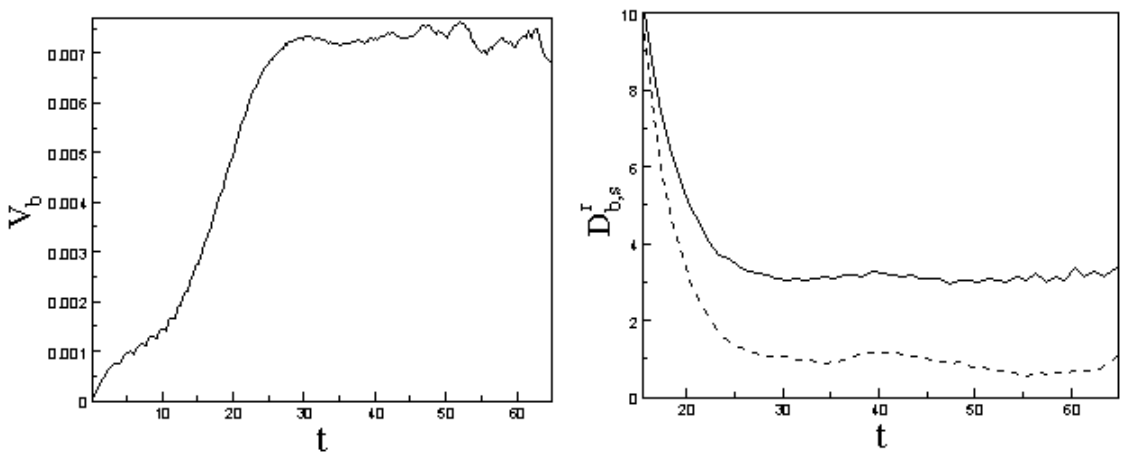

Figure 2.2: Left: The bubble front velocity *vs.* time. Right: Convergence of the drag ratios $D^r_{b,s}$ to a large time asymptotic limit. Rapid small oscillations are suppressed by time averaging of the data. The top line (solid) is D^r_b and the bottom (dashed) is D^r_s. Here $M_2 = 0.05$, $P_{1\infty}/P_0 = 0$, $P_{2\infty}/P_0 = 10$, $\gamma_1 = 4.0$ and $\gamma_2 = 1.1$.

of EOS and compressibility parameters. See also Tables 5.1-5.4 in the Appendix. From (2.14), the phenomenological drag coefficient $\mathcal{C}_i^{s,d}$ in the single mode buoyancy drag equation is related to the terminal velocities and it thus has a similar behavior. However, the solutions are not actually converging to the incompressible limit even within the fairly small Mach numbers we achieve with our compressible code. In Fig. 2.1, we observe that the shape of the bubble fronts at the terminal velocities depends significantly on the EOS parameters for very weakly compressible flows. Continuing this point of view, we see that pressure differences between the two phases are likewise sensitive to EOS and compressibility effects. The same sensitivity of pressure differences on simulation parameters was observed in [53] in the content of multiphase averaged equations.

Let Δp denote the difference $p_2 - p_1$ in the pressures between the two phases, averaged over the horizontal space variable x, as a function of z and t. Then $\Delta p \leq 0$ at the bubble

tip and $\Delta p \geq 0$ at the spike tip. We define $\Delta p_{b,s}$ to be the value of $(-1)^i \Delta p$ at the bubble or spike tip at the time of terminal velocity. Then $\Delta p_{b,s}/\lambda$ is a force, and it can be regarded as a pressure drag force on the bubble/spike tip. These forces display significant EOS and compressibility dependence in the moderate to weak compressibility regime. We dimensionalize this force through division by the form drag force or in view of (2.13) by Ag. Similar definitions apply to Δv and $\Delta v_{b,s}$. Here v_1 (v_2) is the light (heavy) phase velocity averaged over the x space.

Simple results in Table 2.1-2.2 and details in Tables 5.1-5.4 in the Appendix show a significant dependence of the pressure drag force, or the drag ratio on EOS parameters and compressibility,

$$D^r_{b,s} = \frac{\Delta p_{b,s}}{\rho_{s,b}(\Delta v_{b,s})^2} \ . \tag{2.33}$$

The time dependent drag ratios are evaluated at the time of terminal (bubble or spike) velocity. The sensitivity of the drag ratios to EOS parameters results directly from the strong sensitivity of the pressure differences to these parameters. The strongest EOS dependence occurs in Table 5.4 with $P_{1\infty}/P_0 = 10 \gg P_{2\infty}/P_0 = 0$ and for $\gamma_1 = 4.0 \gg \gamma_2 = 1.1$, which is in the four right columns of each table. Generally, the pressure differences and drag ratios decrease as the penetrating phase becomes stiffer (larger γ or P_∞) relative to the ambient phase, and these quantities are much more sensitive to variation of P_∞ than to variation of γ. We also observe that EOS effects are diminished at high compressibility, so that the $M_2 = 0.55$ column of Table 2.1-2.2 is nearly independent of the EOS, in contrast to the EOS dependence, especially of pressure differences and drag ratios for the weakly compressible column $M_2 = 0.05$. In the high compressibility limit, the pressure drag is approximately equal to the form drag.

EOS \ M_2		0.55	0.32	0.1	0.05
$\gamma_1 = 2.0$, $\gamma_2 = 1.1$ $P_{1\infty}/P_0 = P_{2\infty}/P_0 = 0$	M_1	0.29	0.17	0.05	0.03
	C_b	0.31	0.30	0.25	0.25
	C_s	0.43	0.35	0.37	0.36
	D_b^r	1.1	1.2	1.9	2.0
	D_s^r	1.2	1.4	2.9	3.0
$\gamma_1 = 1.1, \gamma_2 = 2.0$ $P_{1\infty}/P_0 = P_{2\infty}/P_0 = 10$	M_1	0.52	0.30	0.10	0.05
	C_b	0.32	0.29	0.25	0.25
	C_s	0.41	0.43	0.39	0.40
	D_b^r	1.1	1.1	2.5	3.1
	D_s^r	1.0	1.0	1.5	1.9

Table 2.1: Dependence of $C_{b,s}$ and drag ratio $D_{b,s}^r$ on compressible EOS parameters.

EOS \ M_2		0.55	0.32	0.1	0.05
$\gamma_1 = 4.0$, $\gamma_2 = 1.1$ $P_{1\infty}/P_0 = 0$, $P_{2\infty}/P_0 = 10$	M_1	0.68	0.39	0.12	0.06
	C_b	0.29	0.32	0.26	0.25
	C_s	0.36	0.39	0.40	0.42
	D_b^r	1.0	1.2	2.5	3.1
	D_s^r	1.2	1.1	1.0	1.0
$\gamma_1 = 1.1$, $\gamma_2 = 4.0$ $P_{1\infty}/P_0 = 10$, $P_{2\infty}/P_0 = 0$	M_1	0.22	0.13	0.04	0.02
	C_b	0.29	0.32	0.30	0.30
	C_s	0.43	0.43	0.40	0.39
	D_b^r	1.2	1.2	1.6	1.4
	D_s^r	1.1	1.6	3.1	3.6

Table 2.2: Dependence of $C_{b,s}$ and drag ratio $D_{b,s}^r$ on compressible EOS parameters. Here P_0 is the pressure at the initial mean interface position. The smallest Mach numbers (the right most column) are approximately 0.02. (See (2.3)).

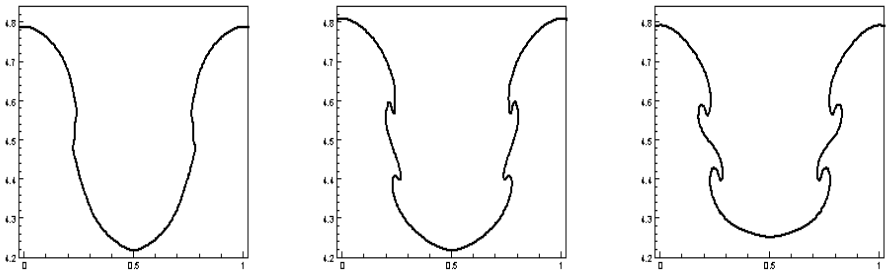

Figure 2.3: 2D single mode RT front plots with different compressibilities (from left to right, $M_2 = 0.32,\ 0.55,\ 0.71$) at terminal velocity. Here γ_i and $P_{i\infty}$ are as in Table 2.3.

2.1.3 Shape Effects on Compressible Mixing Rates

The purpose of this section is to study strong compressibility induced shape effects on mixing rates. We let compressibility M_2^2 vary from 0.1 to 0.8. Over this range, the terminal velocity increases by 10%. We study the radius of curvature and bubble width to understand compressibility induced shape effects. We calculate the radius curvature by fitting a circle to three interface points located at $x = 0.45,\ 0.5$ and 0.55. We see from Table 2.3 a trend for the radius of curvature to increase as the compressibility increases. The maximum bubble width follows the same trend. The minimum bubble width (which can be regarded as defining a maximum spike width) has an opposite trend and is probably not a good predictor of bubble motion. Shape is an important variable in determining drag and terminal velocity, as we see from Fig. 2.3 and the analysis here.

2.2 Effects of Density Variation on Mixing Rates

In this section, we study the effect of compressibility induced density stratification on 3D multimode mixing rates. The chaotic mixing problem differs from the single mode problem in that considerably longer solution times and penetration distances are needed

M_2	C_b	$k = 1/R$ at $V_b = V_b^\infty$	bubble width (min)	bubble width (max)
0.32	0.32	7.78	0.54	0.56
0.55	0.29	4.32	0.52	0.61
0.71	0.25	2.89	0.43	0.66
0.89	0.22	2.65	0.38	0.66

Table 2.3: Radius curvature for the parameter values $A = 1/3$, $\gamma_1 = 1.1$, $\gamma_2 = 4.0$, $P_{1\infty}/P_0 = 10$ and $P_{2\infty}/P_0 = 0$. Here $k = 1/R$ is the bubble tip curvature.

to achieve asymptotic self similar scaling. For this reason, density stratification associated with the weakly compressible regime is generally significant, in contrast to the single mode case where the flows have nearly constant density contrast. We develop an analytical model to account for density stratification effects in multimode self similar mixing. From [20], we know that the compressible multimode simulations remain self similar after removal of stratification effects, until a reversal of the Atwood number regime occurs. Here we reach the same conclusion through analytic models. We use the results of §2.1 to postulate that the multimode drag coefficients are not sensitive to weak or moderate compressibility effects and we study the influence of compressibility induced density stratification.

For cylindrical front tips, we assume that $(-1)^i Z_i(t) > 0$ for $t > 0$, the initial mean interface height $Z_i(0) = 0$, and that the mixing zone expands, *i.e.,* $(-1)^i V_i > 0$. Then Eq. (2.11) reduces to the equation

$$(-1)^i \ddot{Z}_i = Ag - (-1)^i \frac{L_i}{2} \frac{\mathcal{C}_i^{m,d} V_i^2}{Z_i} \ , \tag{2.34}$$

where the multimode drag coefficient $\mathcal{C}_i^{m,d}$ is given in (2.12). Let $S_i = V_i^2/Z_i$. Then S_i can be regarded as a function of Z_i because $Z_i = Z_i(t)$ is monotone. We obtain

$$\frac{dS_i}{dZ_i} = -\frac{V_i^2}{Z_i^2} + 2\frac{V_i}{Z_i}\frac{dV_i}{dZ_i} \ . \tag{2.35}$$

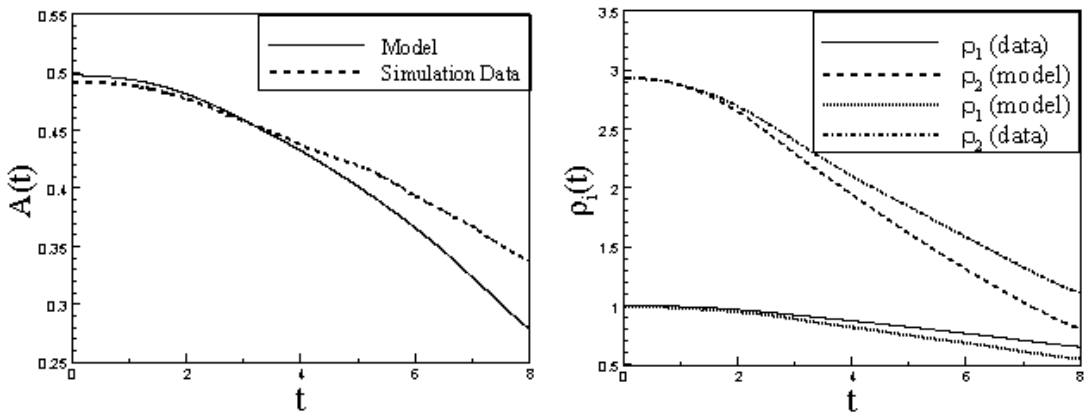

Figure 2.4: Left: Comparison of the model time dependent Atwood number $A_b(t)$ plotted *vs.* time, with direct simulation data. Right: ρ_i at the bubble tip, comparing model and simulation data. Here $M_2^2 = 0.1$ (moderately compressible).

From (2.35), substitution of the identity $\ddot{Z}_i = dV_i/dt = V_i dV_i/dZ_i$ shows

$$Z_i \frac{dS_i}{dZ_i} = -S_i + 2\ddot{Z}_i \ . \tag{2.36}$$

Substituting (2.36) into (2.11), we obtain

$$(-1)^i \frac{1}{2}\left(Z_i \frac{dS_i}{dZ_i} + S_i \right) = Ag - (-1)^i \frac{L_i}{2} \mathcal{C}_i^{m,d} S_i \ , \tag{2.37}$$

i.e.,

$$(-1)^i Z_i \frac{dS_i}{dZ_i} = 2Ag - (-1)^i \left(L_i \mathcal{C}_i^{m,d} + 1 \right) S_i \ . \tag{2.38}$$

We propose a physics model for time dependent Atwood number based on isothermal initial conditions. We assume isentropic flow within the mixing zone. The single phase region has very little flow so that its isothermal initialization property is retained. The density stratification thus satisfies (2.8) for the continuing phase flow at the mixing zone edge and

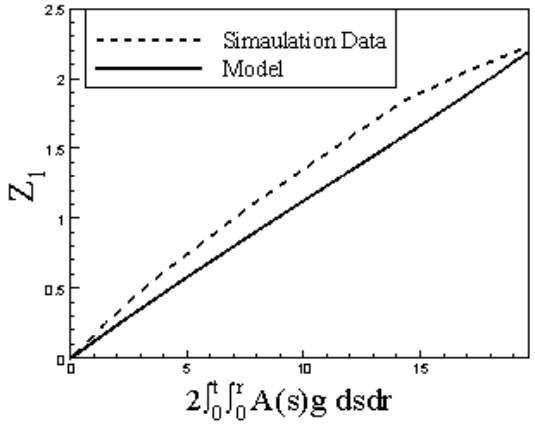

Figure 2.5: Comparison of the model bubble edge with direct simulation data for the $M_2^2 = 0.1$ moderately compressible case. The dashed line represents the simulation data and the solid is calculated from the model equations (2.34) and (2.39). The drag coefficient $\mathcal{C}_1^{m,d}$ in (2.34) is chosen to allow approximate agreement between these curves.

(2.9) for the vanishing flow at the mixing zone edge. From (2.3), the phase i compressibility M_i is a dimensionless length scale over which gravity causes significant fluid compression for fluid i. Motivated by §2.1, we assume that the drag coefficient $\mathcal{C}_i^{m,d} = \mathcal{C}_i^{m,d}(A)$ is independent of M_i, and so we are concerned only with density stratification effects *i.e.,* variable Atwood number effects on the mixing rates. Then $\rho_i \left[\mathcal{T}_i^0 \exp\left(\gamma_{i'} M_{i'}^2 Z_i/\lambda\right) - \mathcal{T}_i^0 + 1\right]^{1/\gamma_i}$ will replace ρ_i and $\rho_{i'} \exp\left(\gamma_{i'} M_{i'}^2 Z_i/\lambda\right)$ will replace $\rho_{i'}$ at the front tip Z_i in the drag-buoyancy equation. Thus only the Atwood number

$$A(Z_i) = (-1)^i \frac{\rho_i \left[\mathcal{T}_i^0 \exp\left(\dfrac{\gamma_{i'} M_{i'}^2 Z_i}{\lambda}\right) - \mathcal{T}_i^0 + 1\right]^{1/\gamma_i} - \rho_{i'} \exp\left(\dfrac{\gamma_{i'} M_{i'}^2 Z_i}{\lambda}\right)}{\rho_i \left[\mathcal{T}_i^0 \exp\left(\dfrac{\gamma_{i'} M_{i'}^2 Z_i}{\lambda}\right) - \mathcal{T}_i^0 + 1\right]^{1/\gamma_i} + \rho_{i'} \exp\left(\dfrac{\gamma_{i'} M_{i'}^2 Z_i}{\lambda}\right)} \tag{2.39}$$

at the bubble or spike tip in (2.38) changes, where $\mathcal{T}_i^0$ is defined in (2.10). In Fig 2.4, we compare this model to numerical data from direct simulation of the multimode mixing [20].

The solid line in the left frame of Fig 2.4 is the model Atwood number plot based on (2.39) using direct numerical simulation data Z_i. We see that the model is qualitatively correct but overstates the influence of density stratification. The difference between the model and the data is caused by two factors. Both heavy and light fluid at the bubble tip in the model are too light relative to the simulation data. The first, and larger, of these effects can be understood as follows. As confirmed from analysis of the 3D multimode simulation data [20], some of the heavy fluid near the bubble tip originated near the $Z = 0$ value for the initial bubble position and was transported there by the bubble motion. This heavy fluid evolves from its $Z = 0$ density isentropically and is heavier than the model assumption. In Fig. 2.5, we compare the edge model (2.34) with the direct numerical data [20]. The solid line represents the solution $Z_1(t)$ of (2.34) with the Atwood number (2.39). Here the drag coefficient in (2.34) is an adjustable parameter, chosen to give the best fit for this comparison. We are here comparing not only the buoyancy drag equation (2.34) to simulation, but also the influence of the model (2.39) or a time dependent Atwood number in this comparison. The exact solution of (2.38) is

$$\begin{aligned} S_i = S_i^{(0)} \exp\left(- \int_0^{Z_i} \frac{L_i(y)\mathcal{C}_i^{m,d} + 1}{y} dy \right) \\ + \int_0^{Z_i} \exp\left(\int_{Z_i}^{y} \frac{L_i(s)\mathcal{C}_i^{m,d} + 1}{s} ds \right) \frac{(-1)^i 2A(y)g}{y}\, dy\,, \end{aligned} \tag{2.40}$$

where $S_i^{(0)} \equiv S_i(Z_i = 0)$, $A(Z_i)$ is given in (2.39) and

$$L_i(Z_i) = 1 - (-1)^i A(Z_i)\ . \tag{2.41}$$

From (2.38), we see that for a finite dS_i/dZ_i at $Z_i = 0$, the initial condition is given as

$$S_i^{(0)} = S_i(Z_i = 0) = (-1)^i \frac{2Ag}{L_i \mathcal{C}_i^{m,d} + 1} = (-1)^i 4\alpha_i Ag \ , \tag{2.42}$$

where $A = A(Z_i = 0)$ and $L_i = L_i(Z_i = 0)$. The integrals in (2.40) are not evaluated explicitly, so we introduce the approximation of (2.39),

$$A(Z_i) \approx A + (-1)^i \frac{(1 - A^2)\, \gamma_{i'} M_{i'}^2 \, (\mathcal{T}_i^0 - \gamma_i)}{2\gamma_i \lambda} Z_i \ , \tag{2.43}$$

valid for small $\gamma_{i'} M_{i'}^2 Z_i / \gamma_i \lambda$, *i.e.*, small Z_i and $M_{i'}$. Suppose that

$$S_i(Z_i) = S_i^{(0)} + S_i^{(1)} Z_i \tag{2.44}$$

for small Z_i . We substitute (2.43) and (2.44) into (2.38) and equate terms of the same order of Z_i. Notice that the 0^{th} order terms cancel. Using (2.42), the coefficients of Z_i give the identity

$$S_i^{(1)} = \frac{g(\mathcal{C}_i^{m,d} + 1)\,(1 - A^2)\,\gamma_{i'} M_{i'}^2 \,(\mathcal{T}_i^0 - \gamma_i)}{\gamma_i \lambda (L_i \mathcal{C}_i^{m,d} + 2)(L_i \mathcal{C}_i^{m,d} + 1)} \quad . \tag{2.45}$$

Observe that the sign of $S_i^{(1)}$ depends on the sign of $\mathcal{T}_i^0 - \gamma_i$. We note that if $A = 1$ or $\mathcal{T}_i^0 = \gamma_i$ is satisfied, it follows from (2.45) that $S_i^{(1)} = 0$ and thus a higher order approximation is required for $S_i = S_i(Z_i)$ in (2.44). Assuming that $S_i^{(1)} \neq 0$, we now solve the equation

$$\frac{V_i^2}{Z_i} = S_i^{(0)} + S_i^{(1)} Z_i \tag{2.46}$$

for Z_i . The solution of Eq. (2.46) is

$$Z_i = \begin{cases} \dfrac{S_i^{(0)}}{2S_i^{(1)}} \left[\cosh\left(t\sqrt{S_i^{(1)}} \right) - 1 \right] & \text{if } \ S_i^{(1)} > 0 \\ \dfrac{S_i^{(0)}}{2S_i^{(1)}} \left[\cos\left(t\sqrt{-S_i^{(1)}} \right) - 1 \right] & \text{if } \ S_i^{(1)} < 0 \end{cases} . \tag{2.47}$$

From (2.47), we derive for small $t\sqrt{|S_i^{(1)}|}$,

$$Z_i = \frac{t^2 S_i^{(0)}}{4} \left(1 + \frac{t^2 S_i^{(1)}}{12} + O(t^4 S_i^{(1)2}) \right) . \tag{2.48}$$

This holds for small $t^2|S_i^{(1)}|$, *i.e.,*

$$t^2 \frac{g(1-A^2)\gamma_{i'} M_{i'}^2 |\mathcal{T}_i^0 - \gamma_i|}{\gamma_i \lambda} \ll 1 . \tag{2.49}$$

In the incompressible limit, $M_i = 0$ and $S_i^{(1)} = 0$, Eq. (2.48) gives the asymptotic solution $Z_i = t^2 S_i^{(0)}/4$ which recovers the incompressible flow solution (1.1).

In general, when the ambient fluid is relatively stiffer, then compressibility speeds up the mixing of the penetrating (less stiff) fluid. We classify the relative stiffness of the light and the heavy fluids into three cases when $A \neq 1$ and $\mathcal{T}_i^0 \neq \gamma_i$. Note $\gamma_{i'}^{-1} < 1 < \gamma_i$ always and $\mathcal{T}_1^0 \mathcal{T}_2^0 = 1$ in view of (2.10).

Case 1. Assume

$$\mathcal{T}_1^0 > \gamma_1 . \tag{2.50}$$

This case occurs when the heavy fluid is stiffer than the light fluid. From (2.45), we see that $S_1^{(1)} > 0$ and $S_2^{(1)} < 0$. Thus, (2.48) implies that compressibility makes the bubble edge of the mixing zone grow faster while the spike edge is slower.

Case 2. Assume

$$\gamma_2^{-1} < \mathcal{T}_1^0 < \gamma_1 \ . \tag{2.51}$$

The two fluids are of comparable stiffness. For example, the case $P_{1\infty} = P_{2\infty}$ falls into this category. In this case, $S_1^{(1)} < 0$ and $S_2^{(1)} < 0$, so both the bubble and the spike grow more slowly when compressibility is included in the buoyancy-drag equation.

Case 3. Assume

$$\mathcal{T}_1^0 < \gamma_2^{-1} \ . \tag{2.52}$$

This case occurs when the light fluid is stiffer than the heavy fluid. We obtain $S_1^{(1)} < 0$ and $S_2^{(1)} > 0$ from (2.45). Therefore compressibility makes the spike edge grow faster while the bubble edge is slower.

The results are valid for small $t\sqrt{|S_i^{(1)}|}$, *i.e.,* when (2.49) holds. Numerical simulations of (2.11) (not reported here) show that these early time trends are preserved into later time.

Chapter 3

Rayleigh-Taylor Mixing with Physical Surface Tension

In this chapter, we identify physical and numerical scale breaking phenomena as significant contributors to turbulent RT mixing rates. We determine the influence of surface tension for immiscible fluids in the experiments of Read and Youngs [44, 52] and Smeeton and Youngs [48] to have a 30% effect on the mixing rate. We have previously compared tracked and untracked numerical simulations and determined that numerical mass diffusion has a 100% or larger effect on the mixing rate, using typical levels of grid spacing [20]. Similar conclusions, formulated in terms of a Froude number analysis, are found in [16]. The influence of initial perturbations on the mixing rate has been argued previously [16].

3.1 Dispersion Relations

In order to compare simulations to experiment, we do not attempt to duplicate exactly all experimental conditions. Rather we apply a change of scale, and attempt to duplicate dimensionless parameters which characterize the experiments. The Rayleigh-Taylor experiments are for the most part strongly incompressible, and simulation in this regime is not practical with a compressible code, so we are content with reduction of the dimensionless compressibility to sufficiently small values so that the incompressible limit has been attained numerically. Similarly, we do not attempt to duplicate the very large number of different

Atwood numbers present in the experiments, as the scaling properties of this variable are well understood. Physical values of the scale breaking parameters are available from published sources, especially if we ignore refinements such as temperature dependence for quantities slowly varying over a presumed range of experimental temperatures. See [46] for a discussion of transport coefficients in the plasma regime, where compressibility is also important.

We first introduce the dimensionless mass diffusion $\tilde{\nu}$, surface tension $\tilde{\sigma}$, viscosity $\tilde{\mu}$ and thermal conductivity $\tilde{\kappa}$ constants

$$\begin{aligned} \tilde{\nu} &= \nu/\lambda\sqrt{Ag\lambda}\ , \qquad \tilde{\sigma} = \sigma/\lambda^2\Delta\rho g\ , \\ \tilde{\mu} &= \mu/\lambda\sqrt{Ag\lambda}\ , \qquad \tilde{\kappa} = \kappa/c_p\rho\lambda\sqrt{Ag\lambda}\ . \end{aligned} \tag{3.1}$$

Here $\nu, \sigma, \mu,$ and κ are the corresponding dimensional parameters, c_p is the specific heat and λ is a wavelength characterizing the initial perturbations. The wave length of the initial disturbance is the least well determined of the quantities which enter into the dimensionless scale breaking coefficient. The theory of the most rapidly growing wave length asserts that the observed, or true initial disturbance, in the absence of externally imposed disturbances, will have this most rapidly growing length. The growth rates are determined by dispersion relations, which assume a small amplitude initial disturbance. When considering miscible fluids, we denote the thickness of the diffusion layer as $\delta_D = 2\sqrt{\nu t}$. The dispersion relation for incompressible flow including both viscosity and mass diffusion gives the growth rate [46]

$$n = \left(Agk/\psi + \mu^2 k^4\right)^{1/2} - (\mu + \nu)k^2\ , \tag{3.2}$$

where ψ is the eigenvalue of the equation

$$\frac{d}{dz}\left(\rho\frac{dw}{dz}\right) = wk^2\left(\rho - \frac{\psi}{Ak}\frac{d\rho}{dz}\right)\ , \quad w \to 0 \text{ as } z \to \pm\infty\ ,$$

and

$$\rho = \frac{1}{2}(\rho_1 + \rho_2)(1 + A\mathrm{erf}(z/\delta_D)) \ .$$

is the density profile. The most unstable wavelength can be calculated numerically. When viscosity alone is dominant, the value of λ is determined analytically [46],

$$\lambda = \frac{4\pi\mu^{2/3}}{(Ag)^{1/3}} \ , \tag{3.3}$$

The dimensionless viscosity parameter $\tilde{\mu}$ with this theoretical wavelength is a constant, $\tilde{\mu} = 1/(4\pi)^{3/2}$. The thermal diffusivity ν_0 can be defined by

$$\nu_0 = \frac{\kappa}{\rho c_p} \ ,$$

For incompressible fluids, the thermal diffusivity can be considered as an identical mass diffusion with mass diffusion coefficient ν_0. For immiscible fluids, one has [48]

$$\lambda = 2\pi \left(\frac{3\sigma}{g\Delta\rho}\right)^{1/2}, \qquad \tilde{\sigma} = \sigma/\lambda^2\Delta\rho g = \frac{1}{3(2\pi)^2} = 8.5 \times 10^{-3} \ . \tag{3.4}$$

for all values of g, λ, and $\Delta\rho$.

To clarify the multitude of parameters and their dependences, we have generated a data base of known RT experiments and parameters, an excerpt of which is presented in Table 3.1. We find many cases where the theory of the most unstable wave length agrees with observation. For related experiments of the same class, but lacking the observational data, it seems safe to infer that this theory remains valid. We note that this not only increases the number of experiments which can be modeled by our simulations, but it also removes the slightly subjective aspect of visual determination of the initial wave length.

We also find cases where the observed wave length and the most unstable wave length

do not even nearly coincide. When the observed wave length is different (air-helium [6], hot-cold water [49]), we conclude that the observed value has been imposed by the experimental apparatus. The question of initial conditions for the experimental studies has been widely discussed [16], in the context of arguing that unobserved long wave initial perturbations affect experimentally observed mixing rates α. In contrast, we are making use of observed wave lengths somewhat longer or shorter than the most unstable wave length.

For the case modeled in Chapter 4 of the splitter plate air-helium experiments of Andrews *et al.*, we have as private communication from the author an initial disturbance wave length of 0.5 cm. For those experiments with a series of published visual images, we can estimate an initial wave length as the smallest observable length in the series of images.

A number of experiments have used immiscible fluids with surfactants. There are two issues which require further study in this case: the variable surfactant concentration along the interface between the fluids, and the Marangoni force resulting from variations in surfactant concentration. Until these effects have been modeled numerically, we do not attempt to simulate such experiments.

Plasma accelerated instabilities typically have machined initial perturbations with one or several wave lengths, and visually, it is clear that the dominant effect derives from the imposed wavelengths and not from the most unstable ones. Thus the simulation of instabilities with initial wave lengths other than the most unstable ones is of direct experimental interest, and the effect of scale breaking on these experiments has been identified as an important question [46].

3.2 Methods

We consider seven 3D experiments of Read [44] and six of Smeeton and Youngs [48], for which there is sufficient data to carry out the analysis, which are immiscible and which

Table 3.1: Summary of length scales and scale breaking parameters for various RT turbulent mixing experiments.

Experiment	scale breaking physics	λ observed cm	λ theory cm	parameter observed (dimensionless)	parameter theory (dimensionless)
immiscible [44, 48]	surface tension	0.5	0.4	5.0×10^{-3}	8.5×10^{-3}
miscible [48]	viscosity initial mixing layer	0.38	0.22	4×10^{-4}	9.0×10^{-4}
miscible [49]	viscosity diffusion	5	0.5	8.11×10^{-4}	2.2×10^{-2}
miscible [6]	mass diffusion	0.5	8.37	0.3	4.6×10^{-3}

do not use surfactants. We infer a value of the initial wave length λ from the most unstable wavelength as determined theoretically from a dispersion relation. This value is compared to that obtained by counting numbers of bubbles at an early time, related to the known dimensions of the container. This number is not precisely determined by this method, so the count was performed independently by three people and the results (not very different) were averaged. The resulting experimentally and theoretically determined wave lengths are mostly very similar in those cases where there is sufficient data to carry out the experimental determination. See Table 3.2 and Fig 3.2.

In §3.1, we introduce the dimensionless surface tension $\tilde{\sigma} = \sigma/\lambda^2 \Delta\rho g$, giving an initial $\tilde{\sigma}$ as presented in Table 3.3-3.4. The experiments use a container 15 cm on an edge and have some 30 bubbles (varying between experiments) on the face of the container at an early time in the experiment, giving a bubble diameter $\lambda \approx 15/30$ cm $= 0.5$ cm. At the end of the experiment, the number of bubbles has decreased to about 6 across the face of the container, so that the dimensionless surface tension is 25 times smaller. For the simulation, we consider initial random modes with wave number $8 - 16$, giving rise to about 12 bubbles

along one edge of the computational domain, and thus representing a 5×5 cm^2 portion of the container, with $\tilde{\sigma} = 11$E-3. Other simulations start with $\tilde{\sigma} = 10$E-3 and 7E-3. They end with about 3 bubbles on a face, and $\tilde{\sigma} = 6.7$E-4. The simulation corresponds approximately to the first half of the experiment. The computational grid is $128^2 \times 512$.

Front Tracking is a very convenient framework to add additional surface based physics. Normal vectors and curvature tensors are included in the code. Surface tension forces a pressure jump at the interface proportional to the surface curvature. Within the normal propagation step for the dynamic time step of the front, there is a solution of a Riemann problem. This Riemann problem is central to Front Tracking, as it connects dynamically the states on the two sides of the front; it replaces a finite difference operation across the front. In the Riemann solution the basic equations are equilibration of the normal velocity and the pressure at the front. In the presence of surface tension, with a specified jump in the pressures (proportional to the surface curvature at the point), the equation of pressure equilibration is modified due to the pressure jump. But an equation for the equilibration of the two mid state pressures is still valid, and is used after modification in the usual manner in the solution for the mid state pressures and for the Riemann problem.

We compare these simulations to a typical untracked simulation (conducted previously [20]), see also [16]. Numerical mass diffusion in the untracked simulation reduces the time dependent Atwood number and the observed value of α, both by a factor of about 2 [20].

3.3 Results

Our principal result is the new value for the mixing rate α for the bubble penetration into the heavy fluid. We compare these values to experiments and to a theoretical analysis based on a bubble merger model. In Fig. 4.6, we plot the bubble penetration height h *vs.* Agt^2, for ideal and immiscible tracked simulations and ideal fluid untracked numerically

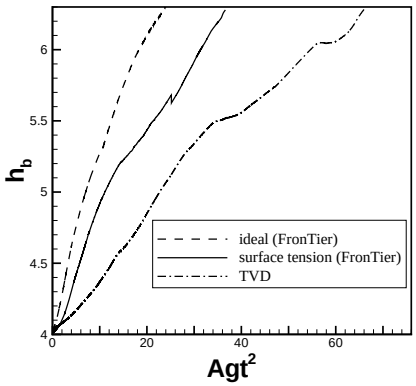

Figure 3.1: The height of bubble penetration is contrasted for three simulations: Ideal fluids, tracked; real fluids (with surface tension), tracked, and ideal fluids, not tracked.

Experiment	Comment	λ_{th} cm	$\tilde{\sigma}_{th}$	λ_o cm	$\tilde{\sigma_o}$
Read-Youngs	Immiscible [44] # 29	0.37	8.5E-3	0.45	5.7E-3
Read-Youngs	Immiscible [44] # 35	0.39	8.5E-3	0.54	4.6E-3
Smeeton-Youngs	Immiscible [48] #104	0.42	8.5E-3	0.41	8.8E-3
Smeeton-Youngs	Immiscible [48] #105	0.45	8.5E-3	0.48	7.3E-3
Smeeton-Youngs	Immiscible [48] #114	0.43	8.5E-3	0.45	7.8E-3

Table 3.2: Comparison of dimensionless surface tension determined by two different definitions of wavelength, theoretical (λ_{th}) and observational (λ_o).

diffusive simulations. The resulting slopes α are given in Table 3.3-3.4.

The factor of two difference ($\alpha = 0.067$ *vs.* 0.035) between experiment and untracked simulations is fully explained by the influence of phenomena which introduce a length scale, and thus break the scale invariance of the Euler equations. That is the result of [20]. Scale breaking causes a lowering of α in simulations. An alternate explanation holds that the experiments have long wave length initial perturbations, causing them to mix more rapidly than they would otherwise. The long wave length perturbations, to the degree that they are present, cause an increase in experimental values of α. These perturbations lower the simulation α required to agree with a hypothetical experiment lacking such perturbations.

Experiment	Comment	α	$\tilde{\sigma}$
Read-Youngs	Immiscible [44] # 29	0.073	8.5E-3
Read-Youngs	Immiscible [44] # 33	0.066	8.5E-3
Read-Youngs	Immiscible [44] # 35	0.071	8.5E-3
Read-Youngs	Immiscible [44] # 39	0.076	8.5E-3
Read-Youngs	Immiscible [44] # 58	0.077	8.5E-3
Read-Youngs	Immiscible [44] # 60	0.073	8.5E-3
Read-Youngs	Immiscible [44] # 62	0.063	8.5E-3
Smeeton-Youngs	Immiscible [48] # 93	0.050	8.5E-3
Smeeton-Youngs	Immiscible [48] # 97	0.060	8.5E-3
Smeeton-Youngs	Immiscible [48] #101	0.063	8.5E-3
Smeeton-Youngs	Immiscible [48] #104	0.066	8.5E-3
Smeeton-Youngs	Immiscible [48] #105	0.072	8.5E-3
Smeeton-Youngs	Immiscible [48] #114	0.060	8.5E-3
Average	$\pm$ 2 STD	0.067 ± 0.015	

Table 3.3: Mixing rates from experiments.

Simulation			
FronTier	Immiscible	0.062-0.055	11E-3
FronTier	Immiscible	0.064-0.058	10E-3
FronTier	Immiscible	0.068-0.061	7E-3
TVD	Ideal Untracked [20]	0.035-0.034	0.0
FronTier	Ideal Tracked	0.09-0.078	0.0

Table 3.4: Mixing rates compared: FronTier simulation compared to experiment and contrasted to untracked (TVD) and ideal fluid FronTier simulations. The two values for simulated α are the average slope and the final slope, $\tilde{\sigma}$ is determined by the theoretical wavelength λ_{th}.

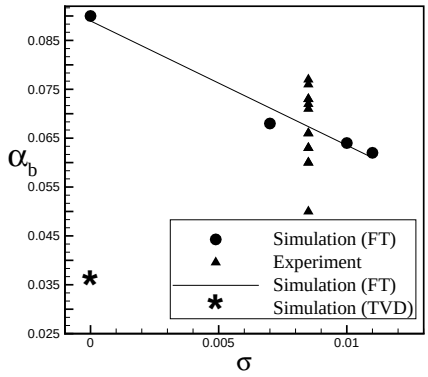

Figure 3.2: The plot of mixing rates α_b *vs.* the dimensionless surface tension $\tilde{\sigma}_{th}$. The line represents the least squares fit to the FT simulation data. The TVD simulation disagrees with experiment by a factor of 2, a result typical of most untracked simulations.

Both explanations must surely have a level of validity, but the relative importance of the two has been up to now an unresolved question. With the present agreement with experiment after correction of scale dependent issues in the simulation, our results suggest that the factor of two discrepancy is resolved and that there is little room for further change from long wave perturbations beyond the scatter present in the experimental data. At least, these perturbations, to the degree that they are present in the experiments and affect mixing rates significantly, require some additional and presently unknown compensating correction.

These two explanations, the scale effects *vs.* the long wave length perturbations in the initial conditions, lead to different physical mechanisms regarding the primary physical processes governing observed turbulent mixing rates. With scale effects corrected, the primary physical mechanism is bubble merger. With the continued increase in bubble size, the natural velocity of the rising bubbles increases. This leads to constant acceleration, and after correction for the extra velocity associated with the fluctuating bubble height, to a bubble merger model [11], and the prediction of $\alpha = 0.06$. The initial perturbation concept leads to the differential growth dynamics of initially imprinted perturbations as the primary mechanism for mixing rate acceleration.

Data/Comment	$\alpha_{\rm b}$	$\alpha_{\rm r}$	$\alpha_{h_{\rm m}}$
Smeeton & Youngs [48]	0.067	0.01	0.028
Cheng *et al.* [11]			
Average #104, 105, 114			
Formula (3.5) [11]	0.0695		
RNG Fixed Point [11]	0.06	0.01	
FronTier immiscible	0.062	0.01	0.034
Formula (3.5)	0.073		

Table 3.5: Comparison of bubble radius and of height fluctuations between experimental data, theory and simulation.

The bubble merger model, moreover, predicts a relation among three different measures of the mixing rate (three different α's). Thus we test this concept and the viability of bubble merger as a primary mechanism in mixing layer acceleration. The three α's are all coefficients of Agt^2. $\alpha = \alpha_{\rm b}$ as in (1.1), refers to the bubble penetration height. $\alpha_{\rm r}$ refers to the bubble radius, and $\alpha_{h_{\rm m}}$ refers to the fluctuations in the bubble height. These three measures of the mixing zone growth rate are related by the formula

$$\alpha_{\rm b} = \frac{1}{2} c_{\rm b} \alpha_{\rm r}^{1/2} + \left[\frac{1}{2k} + \frac{1}{2} \right] \alpha_{h_{\rm m}} \tag{3.5}$$

where $c_{\rm b} = 0.47$ is a Froude number associated with the terminal velocity of a single bubble and $k \approx 0.51$ is a geometrical factor associated with the increase in bubble size due to bubble merger. See [11] for details.

To further test our simulations, we compare the three α's determined from our simulations to those measured from [48], as analyzed in [11] and to the relation (3.5), see Table 3.5.

One might wonder why the bubble merger model agrees with the immiscible experimental value $\alpha = 0.067 \pm 0.015$ rather than the ideal value $\alpha = 0.09$ reported here. In fact, the envelope velocity used in [11] is a phenomenological model tested against experimental data for immiscible fluids, see [30].

In order to carry out the simulation data analysis reported in Table 3.5, we first record local maxima of the interface between the two fluids, in a height range near the height of the leading bubble. The locations of these maxima are the bubble peaks of the simulation. We introduce Voronoi cells about these peaks to define the bubbles themselves (and including the associated spikes), as a decomposition of x, y space. To select local maxima we want to avoid spurious maxima and identify distinct bubbles. For this purpose, we start with an arbitrary local maxima of the light fluid location, within the upper bubble strip defined by the volume fraction $\beta_{\text{light}} \leq 0.25$. This local maxima is accepted if it is unique within a 5×5 stencil of horizontal mesh blocks. In the case of competing maxima within this critical distance, the higher one is selected. This method of selecting local maxima and their heights also determines the height fluctuations of the bubbles. The value thus obtained was compared with that estimated by a manual inspection of the data, and the two were found to agree. For each bubble thus defined, we determine the curve defined by the intersection of the tracked surface with the hyperplane $z = \text{const.}$, and an equivalent radius of a circle having equal area. From this data we find the average bubble radius at a given time. We also considered the radius of the largest circle contained within the cell. See Fig. 3.3 as an illustration of this construction. This definition gives too large a radius for the bubbles as it includes too much of the spike region between the bubbles. Compare to Fig. 3.4 for the location of the light fluid through a fixed slice. We average the minimum and maximum radius for each bubble in this slice and average this over the bubbles to determine the average bubble radius, see Fig. 3.5 and Table 3.5, which also show height fluctuations.

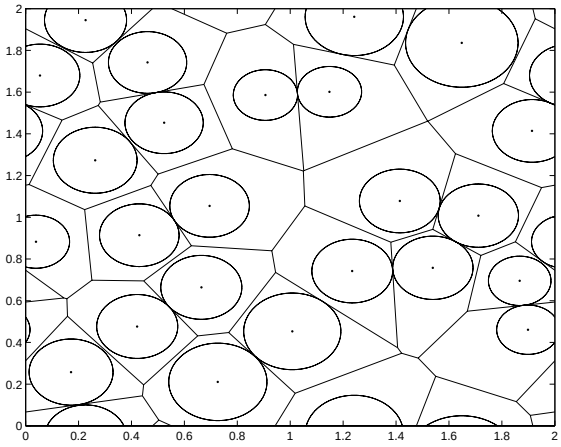

Figure 3.3: Voronoi cell construction about the local bubble maxima to determine equivalent bubble radii based on a slice through the simulation at constant z given by the volume fraction $\beta_{\text{light}} = 0.2$.

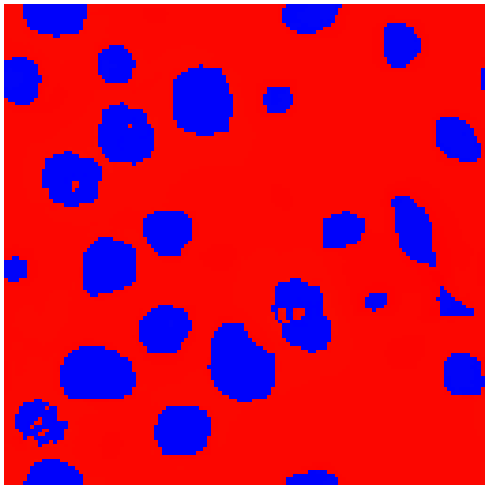

Figure 3.4: Horizontal cross section, showing the bubbles at a height given by the volume fraction $\beta_{\text{light}} = 0.2$, for the same time step as in Fig. 3.3.

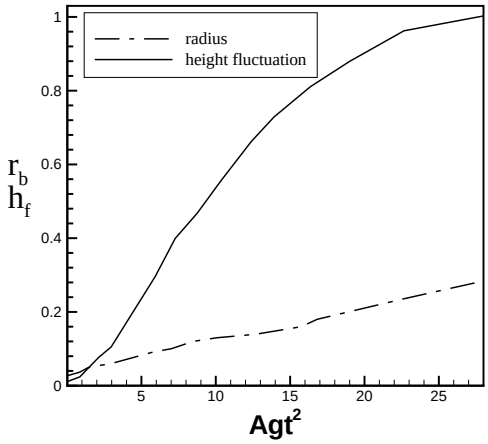

Figure 3.5: Growth of mean bubble width (r_b) and bubble height fluctuations (h_f).

Chapter 4

Rayleigh-Taylor Mixing with Physical Mass Diffusion

The conservation laws

$$\begin{aligned}
&\frac{\partial \rho}{\partial t} + \nabla \cdot \rho \mathbf{v} = \Delta \cdot \nu \rho \ , \\
&\frac{\partial \rho \mathbf{v}}{\partial t} + \nabla \cdot \rho \mathbf{v}\mathbf{v} = -\nabla P + \rho g + \nabla \cdot \nu \mathbf{v} \nabla \rho \ , \\
&\frac{\partial (\rho E)}{\partial t} + \nabla \cdot ((\rho E + P)\mathbf{v}) = \rho \mathbf{v} \cdot g + \nabla \cdot \nu E \nabla \rho \ ,
\end{aligned} \tag{4.1}$$

model the mixing of compressible miscible fluids with physical mass diffusion, where ρ is density, $\mathbf{v}$ is velocity, P is pressure, g is gravity, E is total specific energy, and ν is the coefficient of mass diffusion.

The difficulty in solving this system is to eliminate numerical diffusion across an interface between distinct fluids while allowing the correct amount of physical mass diffusion, in the limit where ν is small relative to the affordable grid resolution. The front tracking method [7, 12, 17, 34, 36, 41] totally eliminates numerical diffusion, but until now it has not allowed the inclusion of small amounts of physical mass diffusion. In this section, we introduce a new algorithm, building on the front tracking method, to add small amounts of physical mass diffusion while preserving the elimination of numerical mass diffusion across an interface. The improved algorithm is based on the analytical solution of the diffusion equation in one dimension.

Our primary results are to introduce the new, limited diffusion tracking algorithm, to test this algorithm in 1D examples, and to discuss its extension to 3D. Sample 3D simulation results with experimental validation will be summarized also. In §4.1 the new algorithm to solve the continuity equation with physical diffusion in one dimension is introduced, making use of the front tracking approach. In §4.2 we present computational verification evidence for the proposed algorithm. In §4.3, we extend the algorithm to higher dimensions. We validate the 3D algorithm by comparing 3D simulations of the Rayleigh-Taylor instability to experimental results.

4.1 Physical Mass Diffusion in One Dimension

The new algorithm, developed first in 1D, is based on the following ideas. Untracked contact discontinuities give rise to a blurred or smeared out front. We preserve the tracking of a sharp front and introduce physical mass diffusion through it as a perturbation. Thus the time step is split into two parts, the first being the usual non diffusive front tracking [18, 26], and the second a purely physical mass diffusion step. Since the first step has been described previously, we only describe the second, physical mass diffusion, step. Conceptually, the front states stored on the tracked front represent the states at $\pm\infty$ relative to the scale of the diffusion layer. For the mass diffusion step at each time step, we compare two algorithms. The first is a subgrid algorithm which allows limited mass diffusion according to the analytic form of the solution for the diffusion equation. The second is a finite difference (FD) algorithm. It is conceptually simpler, and computes the desired diffusion across the front based on the interior (nonfront) states, with no regard for any tracked front which might occur within the difference stencil. After the diffusion layer has reached a width of $2\Delta x$, the first algorithm is turned off and replaced with the second. In referring to the finite difference algorithm, we understand the case in which it is used for all times, not just after

the diffusion layer width is comparable to the mesh spacing. Both algorithms appear to give satisfactory results, but the subgrid algorithm is superior in computing the amount of mass diffused through the interface. These two algorithms are compared to a finite difference algorithm without tracking.

The subgrid algorithm starts with a reconstruction of the diffusion transition layer. Consider the convection equation with physical diffusion

$$\rho_t + u\rho_x = \nu\rho_{xx} \tag{4.2}$$

and the initial condition

$$\rho(x,0) = \begin{cases} \rho_{-\infty} & x < x_0 \\ \rho_{\infty} & x > x_0 \end{cases}$$

where ν is the physical diffusion coefficient. This initial value problem can be solved exactly

$$\rho(x,t) = \rho_{-\infty} + \frac{\rho_{\infty} - \rho_{-\infty}}{\sqrt{\pi}} \int_{-\infty}^{(x-X)/\sqrt{4\pi\nu t}} e^{-\xi^2} d\xi \ , \tag{4.3}$$

where $X = x_0 + ut$.

When Eq. (4.2) is solved numerically, the finite difference (or finite volume) equation is equivalent to the following modified equation

$$\rho_t + u\rho_x = (\nu + \tilde{\nu})\rho_{xx}, \tag{4.4}$$

where $\tilde{\nu}$ is the numerical diffusion. As a result, the numerical solution is approximately

$$\bar{\rho}(x,t) = \rho_{-\infty} + \frac{\rho_{\infty} - \rho_{-\infty}}{\sqrt{\pi}} \int_{-\infty}^{(x-X)/\sqrt{4\pi(\nu+\tilde{\nu})t}} e^{-\xi^2} d\xi. \tag{4.5}$$

The diffusion widths for the exact solution and numerical solution are $d = \pi\sqrt{\nu t}$ and $\bar{d} =$

$\pi\sqrt{(\nu+\tilde{\nu})t}$ respectively. Since $\tilde{\nu} \to 0$ as $\Delta x \to 0$, $\bar{d} \to d$ under the mesh refinement.

However, for a large scale computation in three dimensions, mesh refinement is expensive and requires large increases of memory and CPU time. For example, each doubling of the number of grid points in each dimension requires an 8 times increase of memory and a 16 times increase of CPU time. We wish to use finite and affordable computational mesh to simulate realistic physical mass diffusion when the physical diffusion coefficient is substantially smaller than the numerical diffusion coefficient.

Assume that we know the density transition, $\rho^n_{\pm\infty}$, at the current step, the location of the density transition (midpoint), X^n, at the current step, and the amount of mass which has diffused through the interface in either direction up to the current step, $\mathcal{M}^n_{\pm}$. The density transition and its location are stored as front states and front positions, and updated as part of the (non-diffusive) front and interior state update. The diffused mass, $\mathcal{M}^n_{\pm}$, is a new variable. It is a diffusion progress variable, and it is updated incrementally within the mass diffusion step. On this basis, we define an analytic solution

$$\rho(x,t^n) = \rho_{-\infty} + \frac{\rho_\infty - \rho_{-\infty}}{\sqrt{\pi}} \int_{-\infty}^{(x-X^n)/\sqrt{4\pi\nu t^n}} e^{-\xi^2} d\xi \ . \tag{4.6}$$

The solution of (4.6) depends on a time t^n, defined by the property that the integral of $\rho - \rho_{-\infty}$ from $-\infty$ to X^n is just $\mathcal{M}^n_-$.

Thus we define the current (pseudo) time t^n in terms of $\mathcal{M}^n_{\pm}$ and the current density states at infinity, through the formula

$$\begin{aligned}
\mathcal{M}^n_+ &= \int_0^\infty (\rho(x,t^n) - \rho^n_{+\infty})dx = (\rho^n_{+\infty} - \rho^n_{-\infty}) \int_0^\infty \left(1 - \frac{1}{\sqrt{\pi}} \int_{-\infty}^{\frac{x\sqrt{\pi}}{\sqrt{4\pi\nu t^n}}} e^{-\xi^2} d\xi\right) dx \ , \\
\mathcal{M}^n_- &= \int_{-\infty}^0 (\rho(x,t^n) - \rho^n_{-\infty})dx = \frac{\rho^n_{+\infty} - \rho^n_{-\infty}}{\sqrt{\pi}} \int_{-\infty}^0 \int_{-\infty}^{\frac{x\sqrt{\pi}}{\sqrt{4\pi\nu t^n}}} e^{-\xi^2} d\xi dx \ .
\end{aligned} \tag{4.7}$$

Notice $\mathcal{M}_-^n = -\mathcal{M}_+^n$. The diffused mass at step n is defined as

$$\Delta\mathcal{M}_\pm^n = \mathcal{M}_\pm^{n+1} - \mathcal{M}_\pm^n \ , \tag{4.8}$$

where $\mathcal{M}_\pm^{n+1}$ is defined as in (4.7), but with the pseudo time t^n replaced by $t^n + \Delta t$.

As a convention [13], the diffusion layer is reconstructed as a simple piecewise linear curve, defined by a line segment tangent to $\rho(x, t^n)$ through the transition mid point X^n and cutting the horizontal lines $\rho = \rho_{\pm\infty}$. The edges of the reconstructed transition layer are located at $X^n \pm d^n$, where

$$d^n = d(t^n) = \frac{|\rho_\infty - \rho_{-\infty}|}{2|\max_x \rho'(x, t^n)|} = \pi\sqrt{\nu t^n} = d^{n-1}\sqrt{1 + \frac{\pi^2 \nu \Delta t^n}{(d^{n-1})^2}}$$

and the max is computed within the transition zone.

$\mathcal{M}_\pm^n$ is defined incrementally from its previous value by adding the amount of mass to diffuse in the current step. This amount is defined by the analytic solution of (4.6), using the equivalent time t^n defined in terms of $\mathcal{M}_\pm^n$ and the current time step size Δt. The diffused mass is added to the interior state on one side of the front and subtracted from the interior state on the other.

The subgrid algorithm is applied as long as $d^n < \Delta x$. When $d^n \geq \Delta x$ or if the finite difference algorithm rather than the subgrid algorithm is being used, then the diffusion step is a pure centered second order finite difference step, applied to the interior states, with no regard for the front locations, and no use of ghost cells near the front. In either case, the diffusion step defines an amount of mass to be added to or subtracted from that located in the interior states at locations adjacent to the front.

Assume that the velocity and total energy are slowly varying through the transition layer, in comparison to the density variation. On this basis, we also treat the diffusion

terms added to the momentum and energy equations as a diffusional correction, and define a parabolic update step for these equations.

To update the interior states, we use operator splitting to separate the hyperbolic from the parabolic terms. A regular stencil is one which does not meet the front. The diffusion term is solved by conventional centered finite differences. For an irregular stencil, if the front cuts a mesh cell not at the center of the stencil, we define ghost cell extrapolation of the states on the same side of the front as the center cell using the front states as in [31]. In case the front cuts the central cell of the stencil, *i.e.,* the cell that the stencil is updating, we use the new algorithm explained below. We denote by $\widetilde{\rho}_i^{n+1}, \widetilde{(\rho v)}_i^{n+1}, \widetilde{(\rho E)}_i^{n+1}$ the states at x_i^n after the hyperbolic update. Let $\Delta\mathcal{M}_\pm^n$ be defined as above. This mass must be added to the mass described by the interior states. We distribute this increment of diffused mass to the two closest grid cells which lie on each side of the center of the layer. In order to do this, we detect the closest grid center points on either side of the front center point X_c^{n+1}, namely x_i and x_{i+1}. We add to these cells the mass diffused from the other side

$$
\begin{aligned}
\rho_i^{n+1} &= \widetilde{\rho}_i^{n+1} + \frac{\Delta\mathcal{M}_-^n}{\Delta x} \ , \\
(\rho v)_i^{n+1} &= \widetilde{(\rho v)}_i^{n+1} + \frac{\tilde{v}_i^n \Delta\mathcal{M}_-^n}{\Delta x} \ , \\
(\rho E)_i^{n+1} &= \widetilde{(\rho E)}_i^{n+1} + \frac{\tilde{E}_i^n \Delta\mathcal{M}_-^n}{\Delta x} \ , \\
\rho_{i+1}^{n+1} &= \widetilde{\rho}_{i+1}^{n+1} + \frac{\Delta\mathcal{M}_+^n}{\Delta x} \ , \\
(\rho v)_{i+1}^{n+1} &= \widetilde{(\rho v)}_{i+1}^{n+1} + \frac{\tilde{v}_{i+1}^n \Delta\mathcal{M}_+^n}{\Delta x} \ , \\
(\rho E)_{i+1}^{n+1} &= \widetilde{(\rho E)}_{i+1}^{n+1} + \frac{\tilde{E}_{i+1}^n \Delta\mathcal{M}_+^n}{\Delta x} \ .
\end{aligned}
\tag{4.9}
$$

4.2 Validation

First we compare algorithms for a 1D pure diffusion and transport problem in Fig. 4.1. We set a constant velocity field $v = 0.5$, and study the mass diffusion across a density jump.

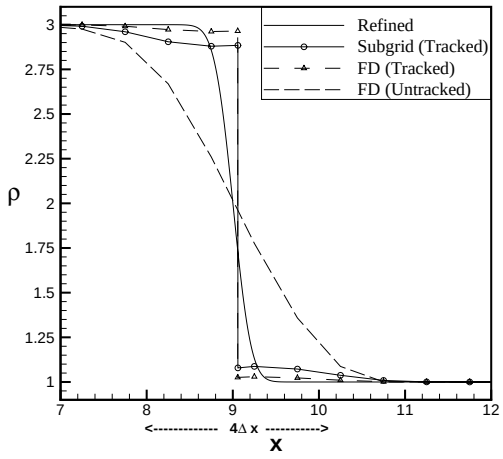

Figure 4.1: Comparison of algorithms for the 1D diffusion and transport problem. Plot of density *vs* time, displayed after 2000 coarse grid time steps and an equivalent physical time for the fine grid.

We compare the exact solution (obtained from a fine grid untracked numerical method) to the subgrid algorithm, the tracked finite difference (FD) algorithm and an untracked finite difference (FD) algorithm. The later three algorithms are computed on a coarse grid, with the final time and the physical values of mass diffusion equivalent to that used in the 3D RT simulation for all figures of Sect. 4.2. We choose $\nu = 0.0008$ in all simulations shown in Sect. 4.2. On the scale of three or so mesh blocks, we see that the untracked algorithm is wrong, the tracked FD algorithm is good and the subgrid algorithm is excellent. The excessive mass diffusion in the untracked solution results from the transport within the Euler equation step and not from the computation of diffusion per se.

Fig. 4.2 compares density contours with different algorithms for the pure transport and diffusion problem, from which we can see that the subgrid (tracked) algorithm is less diffused than the untracked algorithm.

Table 4.1 compares the L_1 errors for different algorithms for the diffusion and transport problem. We denote by $\rho_{\text{exact}}(x, t^n)$ the exact solution, which can be obtained by a numerical

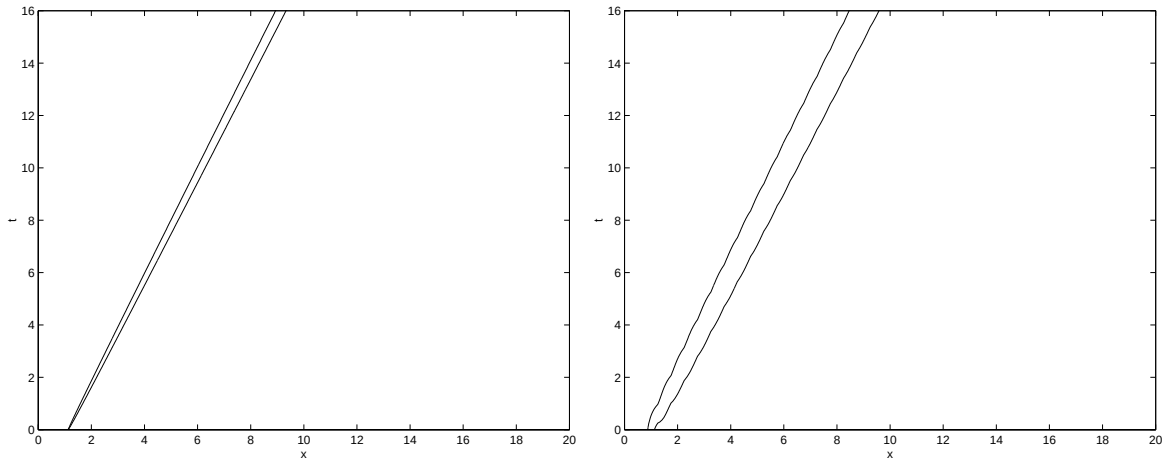

Figure 4.2: Comparison of coarse mesh space time density contours for different algorithms. Two contours are shown, for $\rho = 1.5$ and $\rho = 2.5$, that is 25% and 75% of the density change through the transition layer. To avoid stairstep plots of coarse grid piecewise constant functions, we use reconstruction of the transition layer as defined in Sec. 4.1. For the untracked FD algorithm, we interpolate data between adjacent grid points. Left: subgrid (tracked) algorithm. The diffusion layer has a width of about $2d^n = 0.8\Delta x$ at time $t = 16$. Right: FD (untracked) algorithm. The numerically computed diffusion layer has a width of about $3\Delta x$ at time $t = 16$.

Mesh	Subgrid (Tracked)	FD (Tracked)	FD (Untracked)
40	0.30	0.29	1.02
80	0.28	0.26	0.57
160	0.21	0.20	0.25

Table 4.1: L_1 error comparison for different algorithms.

Mesh	Subgrid (Tracked)	FD (Tracked)	FD (Untracked)
40	0.240	0.071	1.274
80	0.242	0.129	0.735
160	0.252	0.218	0.480
4000	0.264	0.264	0.264

Table 4.2: Comparison of diffused mass for different algorithms at the same time with different grid sizes. The coarsest mesh corresponds to the late time 3D simulation.

solution using a very fine grid and by $\rho(x, t^n)$ the numerical solution computed on a coarse grid, and interpreted as piecewise linear between grid points. For the two tracked algorithms, the grid cell which contains the front is divided into two fractional cells on either side of the front, and the front states provide the additional data to reconstruct a linear solution in each subcell. We calculate the L_1 error at time t^n by $\int_{-\infty}^{\infty} |\rho(x, t^n)_{\text{exact}} - \rho(x, t^n)| dx$.

Table 4.2 compares the mass diffused through the diffusion layer midpoint X^n at time t^n. For untracked simulations, X^n is defined as the midpoint location of the density within the transition layer. This location is, in general, not a grid point, and so the diffused mass calculation involves use of a fractional cell. The diffused mass is computed by $2\int_{-\infty}^{X^n} |\rho(x, t^n) - \rho_{-\infty}| dx$. From this comparison, we see that the subgrid algorithm is far more accurate in this measure of convergence than the FD (tracked and especially untracked) algorithms for a coarse grid. All algorithms agree with a fine grid.

Fig 4.3 shows the convergence of the subgrid and the tracked FD algorithms. Both algorithms have good L_1 error norms, even for the coarse grid, with a slight advantage for

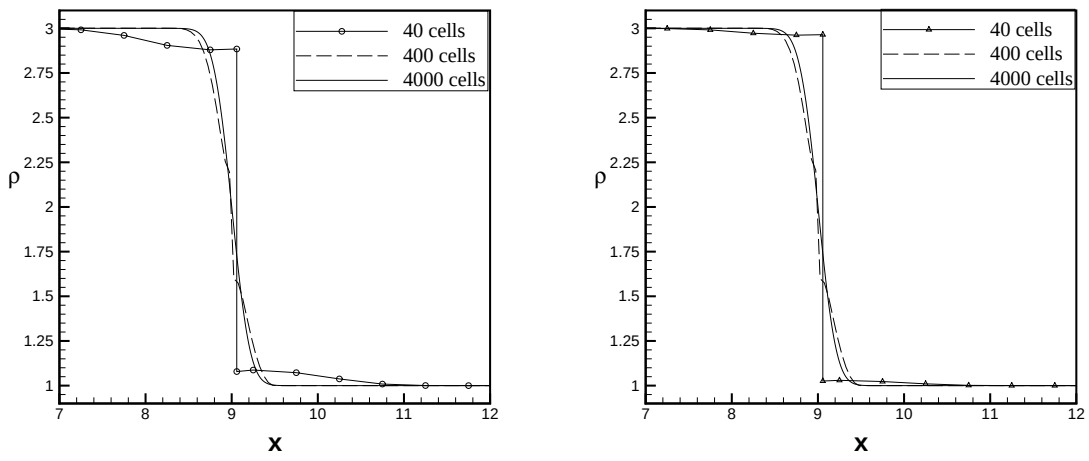

Figure 4.3: Convergence of the tracked subgrid and the tracked FD algorithms for the same 1D diffusion and transport problem. Left: the tracked subgrid algorithm; right: the tracked FD algorithm. The coarsest grid coincides with that of Fig. 4.1.

the FD algorithm.

Fig. 4.4 compares the algorithms for a shock-contact interaction, again with an imposed velocity field. The left frame is before and the right frame after the interaction of the shock with the contact. The same three algorithms are compared to a fine grid solution. Fig. 4.5 compares the numerical algorithms before (left) and after (right) a rarefaction wave interacts with the contact interface, parameters chosen as above. From these three plots, we conclude that the tracked subgrid algorithm and the tracked FD algorithm are nearly equivalent, and both are much better than the completely untracked solution.

4.3 Simulation Results for Miscible Fluids

For the higher dimension case, we split the front into normal and tangential directions. The subgrid algorithm is applied along the normal direction, and no diffusion is added to the tangential sweep. In this way, the subgrid algorithm in one dimension can be extended

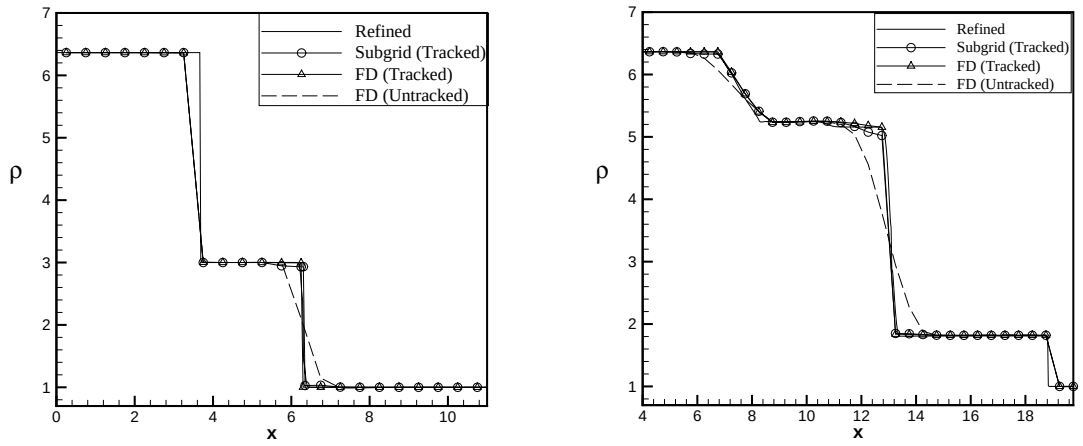

Figure 4.4: 1D comparison of algorithms for a shock contact interaction problem. Left: before the shock interacts with the contact; right: after the shock passes through the contact.

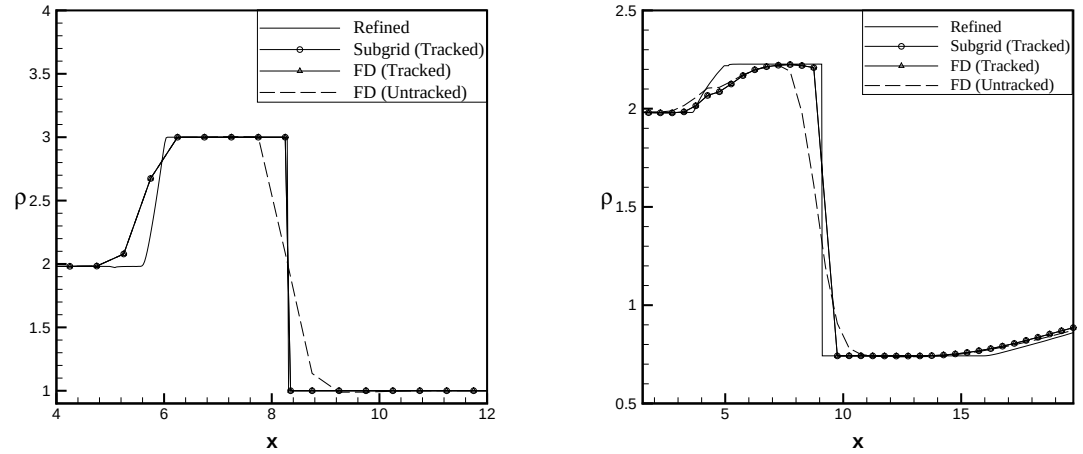

Figure 4.5: 1D comparison of algorithms for a rarefaction contact interaction problem. Left: before the rarefaction interacts with the contact; right: after the rarefaction passes through the contact.

easily and efficiently to the higher dimension. We do not present results from a 3D extension of the tracked FD algorithm, but we remark that it also must be solved in normal-tangential coordinates to avoid over-diffusing the mass. The subgrid algorithm is validated by comparing a 3D simulation of the Rayleigh-Taylor (RT) instability to laboratory experiments [6].

We model miscible fluids using physical values for the interfluid mass diffusion. Experiments [6] studied the mixing of air and helium, with a Fickian diffusion constant $\nu = 0.00066$ cm^2/ms [14]. The dimensionless diffusion constant is introduced in §3.1, $\tilde{\nu} = \nu/\lambda\sqrt{Ag\lambda} = 0.3$, with $g =$ earth's gravity, $A = 0.035$ the Atwood number, and $\lambda = 0.5$ the initial bubble diameter. We model this experiment with an initial $\tilde{\nu} = 0.3$ and we use the Atwood number $A = 0.5$.

Our main results, summarized in Table 4.3, are the values for the mixing rate α for the bubble penetration into the heavy fluid, in agreement with experimental data. One simulation presented here is highly compressible ($M^2 = 0.25$). All the others are nearly incompressible ($M^2 = 0.0076$). Here $M^2 = \lambda g/c_h^2$ is a dimensionless measure of compressibility, where c_h denotes the sound speed of the heavy fluid. On the basis of the results of Table 4.3, we identify scale dependent phenomena, i.e. transport, surface tension and compressibility, as significant contributors to the mixing rate.

We remove the effects of compressible density stratification and of various levels of numerical and/or physical mass diffusion, and explain the various bubble penetration curves in terms of a universal theory, through the use of time dependent Atwood numbers [20]. The raw or unadjusted mixing rate is the slope of the curve h vs. Agt^2. Following [20], we introduce a time dependent Atwood number $A(t)$ defined by the solution itself. Using this, we can define the variable density corrected mixing rate as the slope of h vs. $2\int_0^t \int_0^s A(r)g dr ds$.

The raw and density renormalized mixing rates are plotted in Fig. 4.6 (left and right). Observe that the rescaled plots on the right, for two tracked simulations (ideal and physical

Table 4.3: Mixing rates compared: FronTier simulation compared to experiment; ideal fluid FronTier compared to ideal untracked TVD. The final column (computed for simulations only) is the percentage change from the FronTier simulation of the ideal case.

Experiment Simulation	Comment	Coeff.	α	Percentage change
Banerjee-Andrews	Mass diffusion [6]	$\tilde{\nu} = 0.3$	0.07	
FronTier	Miscible	$\tilde{\nu} = 0.3$	0.069	-23%
TVD	Untracked [20], Ideal	0.0	0.035	-61%
FronTier	Ideal	0.0	0.09	0%
TVD	Untracked, ideal (renormalized)	0.0	0.076	-16%
FronTier	Miscible, ideal (renormalized)	0.0	0.089	-1%
FronTier	High compressibility (renormalized)			
	ideal, $M^2 = 0.25$	0.0	0.11	+22%
	ideal, $M^2 = 0.5$ [20]	0.0	0.21	+133%

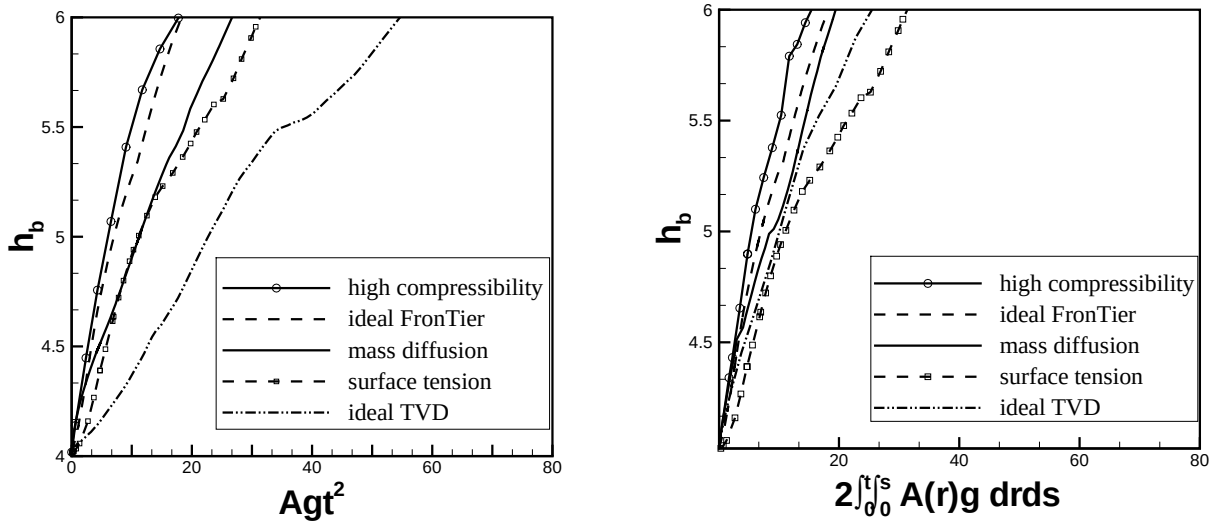

Figure 4.6: Left: Self similar growth of the mixing zone. Right: The same data plotted using a time dependent Atwood number, to remove the effects of numerical or physical mass diffusion and of compressible ($M^2 = 0.25$) density stratification. See also Table 4.3 where results from several different compressibilities are given.

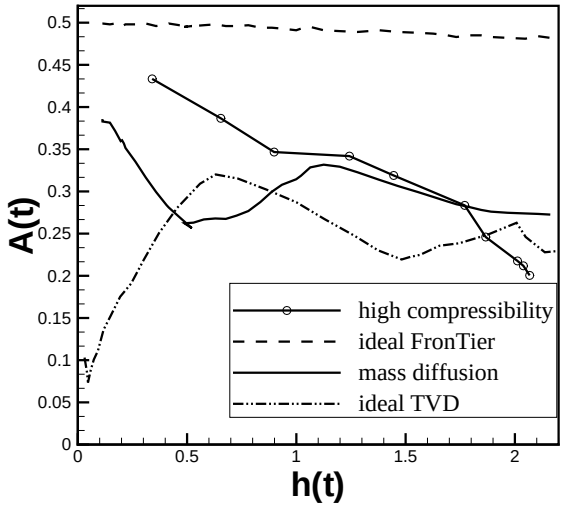

Figure 4.7: Plot of the time dependent Atwood number for tracked simulations with and without physical mass diffusion and for an untracked simulation (with numerical mass diffusion).

mass diffusion), are in close agreement, indicating that the differences in the time dependent Atwood number account for the different penetration rates of these cases. The discrepancy between scaled tracked and untracked renormalized plots appears to be due to grid related interface smoothing, an effect we call numerical surface tension. The discrepancy between scaled tracked high and low compressibility is due to compressibility effects.

The h vs. Agt^2 and especially the renormalized h vs. $\int_0^t \int_0^s A(r)gdrds$ plots in Fig. 4.6 have straight line shapes after an initial transient, and we here report the slope obtained by joining the initial to the final point. We separate variable density effects from the numerical and physical surface smoothing and surface tension effects and obtain the results of Table 4.3.

In Fig. 4.7, we plot the time dependent Atwood numbers [20] for the curves of Fig. 4.6. The deviation of the low compressibility $A(t)$ from $A = A(t = 0)$ is due mainly to numerical or physical mass diffusion.

4.3.1 The Bubble Merger Process

The acceleration of the bubble envelope in multimode Rayleigh-Taylor (RT) instability is postulated to depend on the process of bubble competition and merger [5, 11, 35, 39, 47, 54]. Key phenomena characterize this process:

1. Proximity of bubbles to each other. Bubble competition and the merger which drives the acceleration of the bubble envelope can only occur if bubbles are sufficiently close to each other.

2. Speed of taller vs. shorter bubbles. Taller bubbles should on the average advance faster than neighboring shorter bubbles. These faster moving bubbles then expand to take up the space left by the slower, lower bubbles which, in terms of relative velocities, get swept downstream of the main bubble envelope flow. Thus there is an inverse cascade with fewer and larger structures dominating the flow as time progresses. This process is called bubble competition and merger.

3. Speed of taller bubbles vs. single mode theory. The vertical velocity of the taller multimode RT bubbles should be considerably greater than the terminal velocity of a single bubble of an equivalent radius in single mode RT instability. The increment in velocity, called the bubble envelope velocity [30], is about equal to single mode bubble velocity [30].

We demonstrate quantitatively (with the low compressibility simulation of Sec. 4.3) that tracked mass diffusive simulations exhibit these three characteristics. Our diagnostics therefore support the view that bubble competition and merger occurs in RT simulations, driving the acceleration of the bubble envelope.

4.3.2 Multimode vs. Single Mode

Since Eq. (1.1) is used to describe the bubble penetration in multimode RT instability, it is important that the simulations remain in the multimode regime up to the latest times that Eq. (1.1) is used to model the bubble envelope growth. The dynamics of single mode RT instability are very different from the multimode case. Single mode RT instability is characterized by a brief initial period of exponential growth followed by linear acceleration and then transition to an approximately constant terminal velocity, v_∞, of the bubble [29, 39, 47, 52]; multimode RT is characterized by nonlinear coupling of modes which drives continual acceleration of the bubble envelope.

To analyze the bubble dynamics, we first identify the x, y (horizontal) plane location of the bubble peaks, then determine the average of the number of bubbles near each bubble. We use an algorithm described in [22] to determine distinct bubble peaks above the 20% light fluid volume fraction height. To ensure the accuracy of these bubble peak locations, we compare the results of the algorithm with horizontal slices through the bubble portion of the mixing zone at and above the 20% light fluid volume fraction height. This combined approach gives accurate bubble tip locations up to time 18 (the simulation runs up to time 21), but the extremely complicated nature of the late time interface makes the task of identifying individual bubbles highly subjective, and none of the analysis described in this section is performed on simulation times later than $t = 18$.

The radius of influence (or radius) of a bubble is defined by first considering a Voronoi cell decomposition of the horizontal plane containing the $x - y$ location of the bubble peaks. The radius of the largest circle centered at a bubble location and enclosed in its Voronoi cell defines the radius of that bubble. Fig. 4.8 (a) illustrates this construction for $t = 15$. See also [22].

We use a one bubble radius separation to determine the number of bubbles near a given

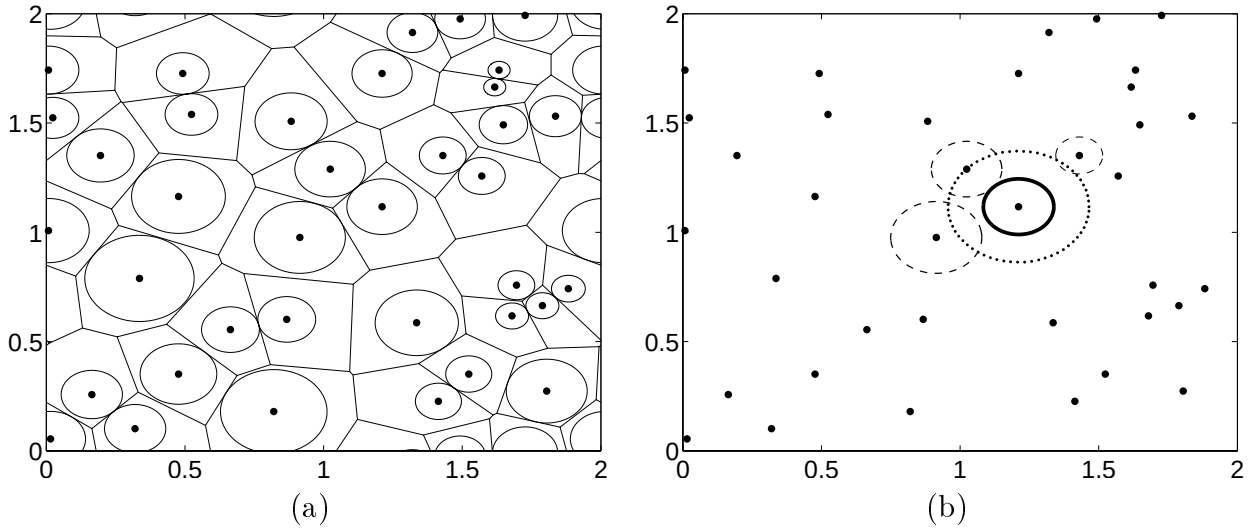

Figure 4.8: Horizontal plane view of bubble tip locations at time $t = 15$. (a) Voronoi diagram of the bubble tip locations in the horizontal plane, and the accompanying maximum radius circles enclosed in a Voronoi cell and centered at a bubble tip. These circles represent the bubbles. (b) Definition of the 1-radius neighborhood of a bubble; the inner circle (solid line) is the bubble as defined in (a) while the outer circle (dotted line) defines a 1-radius neighborhood around that bubble. The three dashed line circles represent bubbles within the 1-radius neighborhood of the solid line bubble, and thus presumed to interact with it.

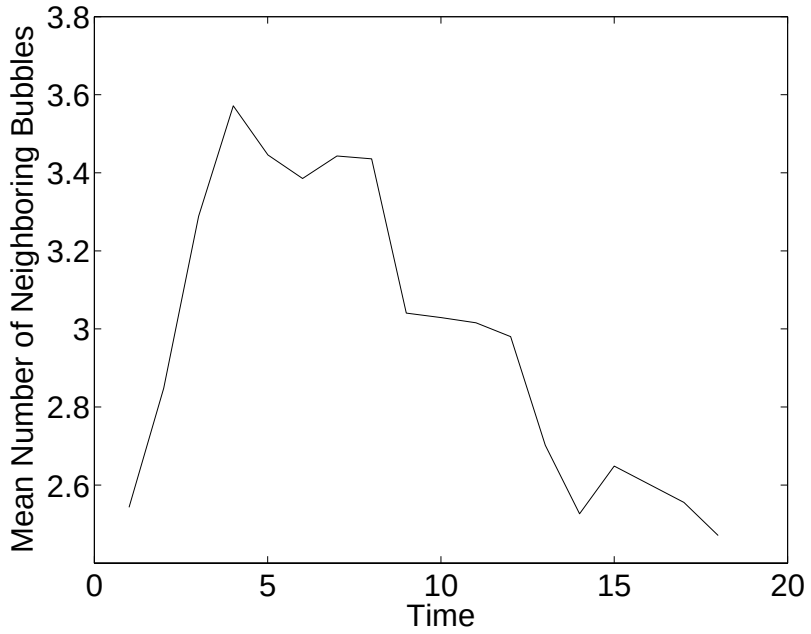

Figure 4.9: Mean number of bubbles within a 1-radius neighborhood of a given bubble.

bubble. See Fig. 4.8 (b). In Fig. 4.9, we plot the average number of other bubbles within a 1-radius neighborhood of each bubble. The average is about 3, showing that the multimodal regime is still present at late time. Bubbles are still sufficiently close to each other at late time to affect the growth pattern of other bubbles significantly; bubble competition and merger is still viable. This analysis quantitatively confirms the qualitative impression obtained from late time front plots of tracked RT multimode simulations. (See, for example, [23] or [21].)

4.3.3 Vertical Velocities of Neighboring Bubbles and the Inverse Cascade

Using the 1-radius neighborhoods defined in Sec. 4.3.2 for each bubble, we study the relationship between the vertical velocities of neighboring bubbles. The bubble competition and merger concept requires that, in general, taller bubbles advance faster than their

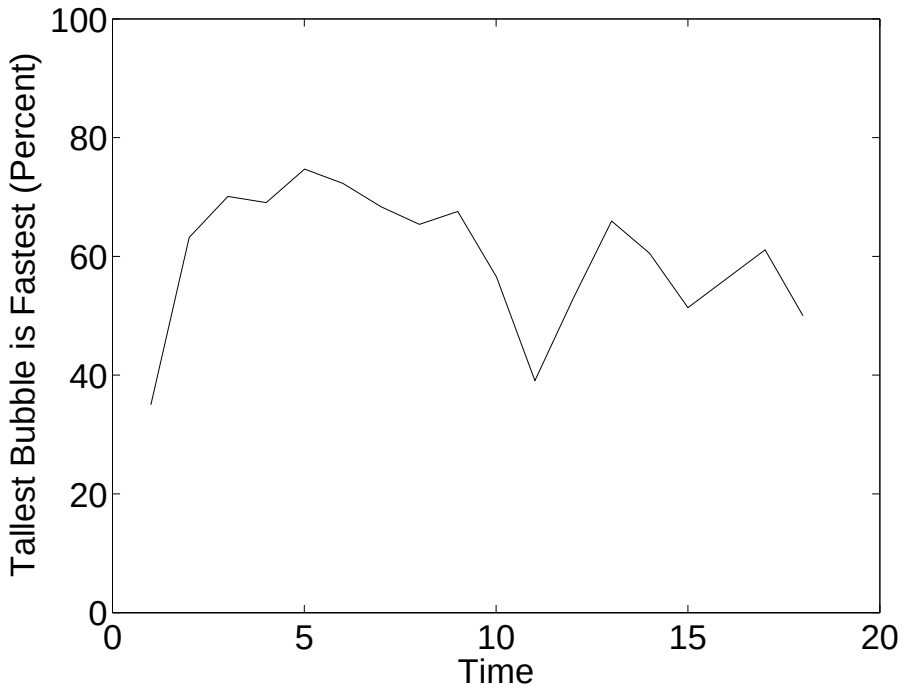

Figure 4.10: Percentage measure of the number of times the tallest bubble in a neighborhood is also the fastest advancing bubble in that neighborhood.

shorter neighbors. We illustrate that this in fact happens in our front tracking mass-diffusion simulation using two metrics.

First, in Fig. 4.10, we show as a function of time the percentage of occurrences of the tallest bubble in a neighborhood also having the largest vertical speed. This percentage (about 60% on a time-averaged basis) can be compared with the value 25% which would result if there were no correlation between bubble height and velocity.

However, even if the tallest bubble in a neighborhood is not the fastest advancing bubble, it is typically *almost* the fastest bubble. A second metric also illustrates that taller bubbles move faster than shorter ones. For each 1-radius neighborhood we determine the percentage of bubbles which are slower than the tallest bubble in that neighborhood. The weighted mean of those percentages (with the proportion of the total number of neighborhood

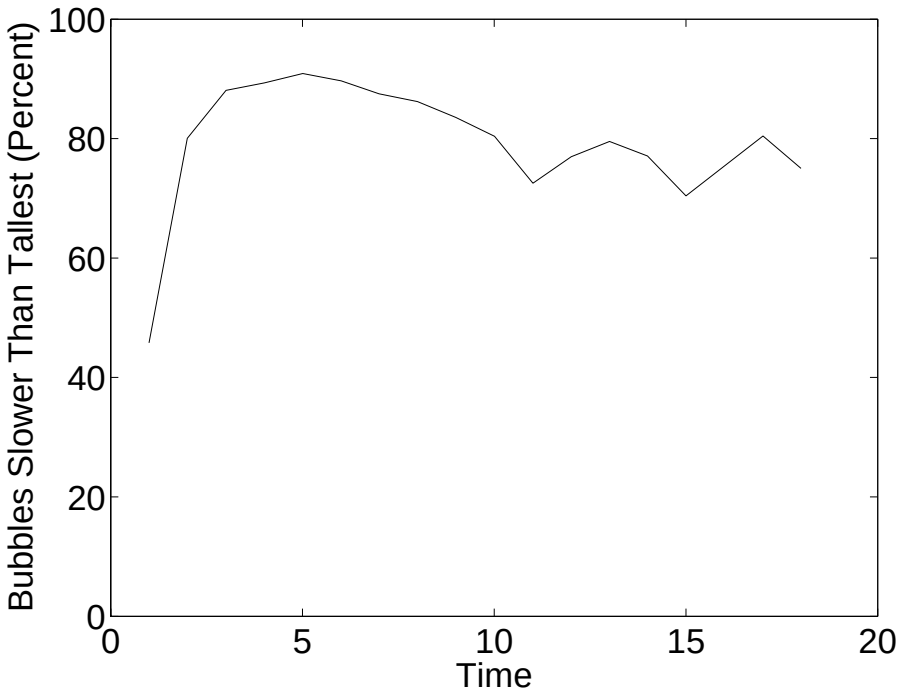

Figure 4.11: The percentage of bubbles in a neighborhood which are slower than the tallest bubble in that neighborhood.

bubbles in each neighborhood serving as the weights) is then computed at fixed time for all 1-radius neighborhoods of bubbles. The results are summarized in Fig. 4.11. The tallest bubble typically moves faster than 80% of its neighbors. In the absence of a speed-height correlation, this value would be 50%. We therefore have quantitative confirmation that taller bubbles generally advance faster than do shorter ones in our simulation, as is characteristic of the process of bubble competition and merger.

Finally, we provide evidence that the disparity in bubble speeds results in an inverse cascade of increasing bubble sizes and decreasing number of structures having a larger size in the bubble envelope. In Fig. 4.12, the plots show, as a function of simulation time, a decreasing trend in the number of bubbles (frame (a)) and an increasing trend in the mean radius, $\bar{r}$, of the bubbles (frame (b)). Reference [11] defines an $\alpha_r = \bar{r}/Agt^2$ for which there is

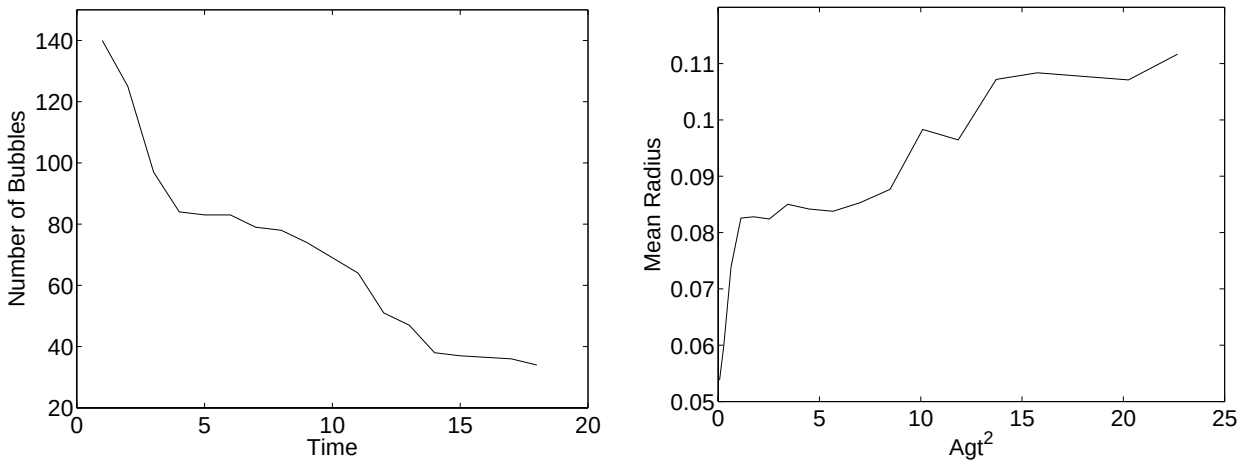

(a) (b)

Figure 4.12: (a) The number of bubble peaks above the 20% volume fraction contour as a function of time. (b) The mean bubble radius, $\bar{r}$, as a function of scaled distance.

no known published miscible experimental value but for which the immiscible experimental value is approximately 0.01. The immiscible simulation [22] reports $\alpha_r = 0.01$ also. That value is twice as large as $\alpha_r = 0.005$ obtained from the miscible front tracking simulation, indicating a possible difference in the bubble dynamics between miscible and immiscible RT mixing.

4.3.4 Multimode Velocities vs. Single Mode Terminal Velocities

We compare the vertical speeds of the taller multimode RT simulation bubbles to the terminal speeds of single mode bubbles of equivalent radii. By $t = 2$, the simulation bubbles have achieved a height much greater than half their mean radius. From the rough guideline established in [52], this means that as single mode perturbations they should be entering the terminal velocity regime. However, on average, the speed of the tallest 25% of the multimode simulation bubbles is 2.4 times the corresponding single mode terminal velocity. This is consistent with the two-dimensional simulation study [30], which found increases in multimode

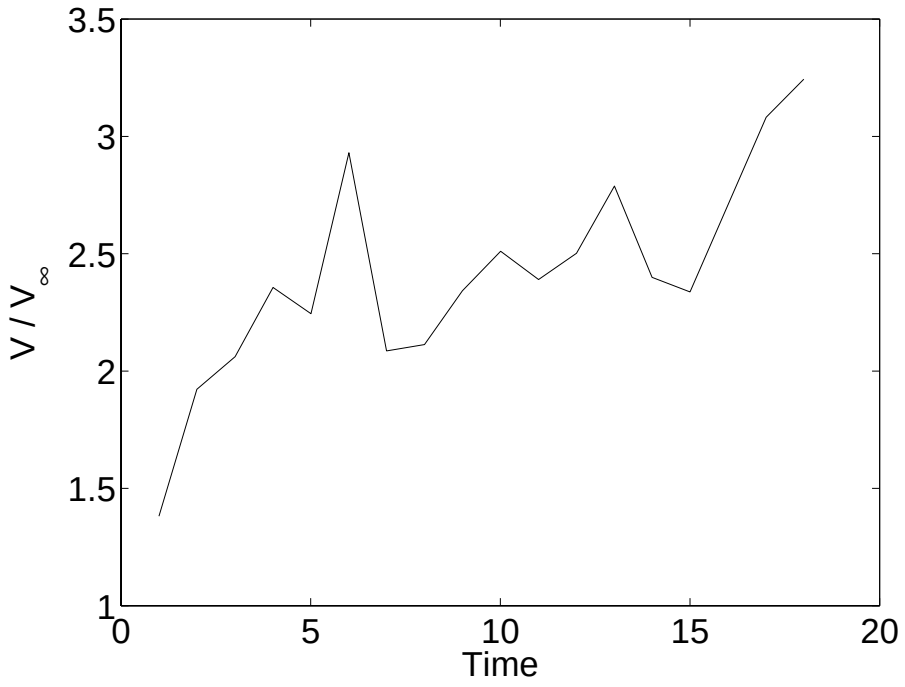

Figure 4.13: A comparison of the front tracking simulation vertical speed, v, of the tallest 25% of bubbles with the Taylor-formula terminal vertical speed, v_∞, of those same bubbles when regarded as single isolated bubbles.

bubble velocities by a factor of 2 over equivalent single mode bubble terminal velocities. This is further evidence that the bubble dynamics are dominated by the interaction of neighboring bubbles. These results are summarized in Fig. 4.13. The formula used for computing v_∞ [50] is

$$v_\infty = c_b\sqrt{Agr} = 0.48(\sqrt{Agr}), \tag{4.10}$$

where r is the bubble radius.

Chapter 5

Conclusions

We find insensitivity of Froude numbers and drag coefficients to compressibility and EOS parameters, but in contrast a strong dependence of shape and pressure differences on these same qualities. For multimode mixing, the dominant compressibility effect is due to compressibility induced density stratification of the fluids.

We have reported on a new set of 3D Rayleigh-Taylor chaotic mixing simulations, based on a new tracking algorithm in the Front Tracking code FronTier. We include a discussion of other scale breaking physical effects: mass diffusion, surface tension, compressibility, and numerical scale breaking effects: numerical mass diffusion and effective numerical surface tension in the analysis. The scale breaking terms cause a change in the mixing rate α ranging from over $+100\%$ to -61% in comparison to an ideal simulation, lacking scale breaking effects. They agree with experimental values for both miscible and immiscible fluids. Accurate numerical tracking to control numerical mass diffusion and accurate modeling of physical scale breaking phenomena (surface tension or mass diffusion) were the critical steps for this level of agreement.

A broader conclusion of this thesis is to document the sensitivity of Rayleigh-Taylor mixing rates to physical and numerical scale breaking phenomena and to scale breaking diffusive or interface smoothing artifacts of the numerical algorithms used in simulations.

Since Rayleigh-Taylor phenomena occurs on a variety of scales, from laser fusion to turbulent combustion in a supernova, modeling of scale breaking phenomena in the physics and eliminating it from the numerics becomes an issue.

Remaining issues concern the data of Dimonte and Schneider [15], for which the role of surfactants requires additional physical modeling and some miscible experiments for which viscosity, not mass diffusion, is the dominant scale breaking physics. Additionally, the influence of mesh refinement should be explored when computer resources permit, but we observe that the mesh resolution per bubble used in the present study is already 2 times finer than that of the benchmark study [16].

Appendix: EOS Dependence of the Froude number and Drag Ratio in the Weakly Compressible Limit

In Tables 5.1-5.4 we show that dependence of $C_{b,s}$ and the drag ratio $D^r_{b,s}$ on the EOS. Here $M_2 = 0.1$ and P_0 is the pressure at the initial mean interface position.

$\gamma_2 \backslash \gamma_1$	$M_1,\ C_b,\ C_s,\ D_b^r,\ D_s^r$		
	1.1	2.0	4.0
1.1	0.07, 0.25, 0.39, 2.0, 2.0	0.05, 0.25, 0.37, 1.9, 2.9	0.04, 0.27, 0.35, 1.0, 4.0
2.0	0.10, 0.26, 0.40, 2.5, 1.5	0.07, 0.25, 0.39, 2.0, 2.0	0.05, 0.25, 0.37, 1.6, 3.0
4.0	0.13, 0.26, 0.42, 2.5, 1.0	0.10, 0.25, 0.40, 2.5, 1.5	0.07, 0.25, 0.39, 2.0, 2.0

Table 5.1: $P_{1\infty}/P_0 = P_{2\infty}/P_0 = 0$.

$\gamma_2 \backslash \gamma_1$	$M_1,\ C_b,\ C_s,\ D_b^r,\ D_s^r$		
	1.1	2.0	4.0
1.1	0.07, 0.25, 0.39, 2.0, 2.0	0.05, 0.25, 0.38, 1.8, 2.7	0.04, 0.26, 0.35, 1.0, 3.7
2.0	0.10, 0.25, 0.39, 2.5, 1.5	0.07, 0.25, 0.39, 2.0, 2.0	0.05, 0.25, 0.37, 1.6, 3.0
4.0	0.13, 0.26, 0.41, 2.5, 1.0	0.10, 0.26, 0.40, 2.5, 1.5	0.07, 0.25, 0.38, 2.1, 2.1

Table 5.2: $P_{1\infty}/P_0 = P_{2\infty}/P_0 = 10$.

$\gamma_2 \backslash \gamma_1$	$M_1,\ C_b,\ C_s,\ D_b^r,\ D_s^r$		
	1.1	2.0	4.0
1.1	0.23, 0.26, 0.43, 2.5, 0.6	0.17, 0.26, 0.42, 2.5, 0.9	0.12, 0.26, 0.40, 2.5, 1.0
2.0	0.32, 0.26, 0.44, 2.5, 0.5	0.23, 0.26, 0.42, 2.5, 0.5	0.17, 0.26, 0.41, 2.5, 0.9
4.0	0.45, 0.26, 0.44, 2.5, 0.4	0.33, 0.26, 0.44, 2.5, 0.5	0.23, 0.27, 0.44, 2.5, 0.6

Table 5.3: $P_{1\infty}/P_0 = 0$ and $P_{2\infty}/P_0 = 10$

$\gamma_2 \backslash \gamma_1$	$M_1,\ C_b,\ C_s,\ D_b^r,\ D_s^r$		
	1.1	2.0	4.0
1.1	0.02, 0.36, 0.39, 0.7, 5.2	0.016, 0.40, 0.40, 0.5, 4.9	0.01, 0.49, 0.40, 0.02, 6.8
2.0	0.03, 0.33, 0.40, 1.1, 4.0	0.02, 0.36, 0.40 , 0.6, 5.0	0.015, 0.43, 0.40, 0.2, 6.0
4.0	0.04, 0.30, 0.40, 1.6, 3.1	0.03, 0.32, 0.39, 1.0, 3.5	0.02, 0.37, 0.39, 0.5, 5.4

Table 5.4: $P_{1\infty}/P_0 = 10$ and $P_{2\infty}/P_0 = 0$.

Bibliography

[1] S. Abarzhi and A. Oparin. Three-dimensional bubbles in Rayleigh-Taylor instability. *Phys. Fluids*, 11(11):3306–3311, 1999.

[2] S. I. Abarzhi. Bubble symmetry in the Rayleigh-Taylor instability. *Physica Scripta*, 56(4):296–297, 1999.

[3] S. I. Abarzhi, J. Glimm, and An-Der Lin. Rayleigh-Taylor instability for fluids with a finite density contrast. *Phys. Fluids*, 15:2190–2197, 2003.

[4] S. I. Abarzhi, J. Glimm, and K. Nishihara. Rayleigh-Taylor instability and Richtmyer-Meshkov instabilities for fluids with a finite density contrast. *Phys. Lett. A*, 11:1–7, 2003.

[5] U. Alon, J. Hecht, D. Ofer, and D. Shvarts. Power laws and similarity of Rayleigh-Taylor and Richtmyer-Meshkov mixing fronts at all density ratios. *Phys. Rev. Lett.*, 74:534–538, 1995.

[6] A. Banerjee and M. J. Andrews. A gas channel facility to investigate statistically steady Rayleigh-Taylor mixing at high Atwood numbers. *Phys. of Fluids*, 2005. Manuscript for Phy. of Fluids.

[7] M. Ben-Artzi. The generalized riemann problem for reactive flow. *J. Comp. Phys.*, 86:70–101, 1989.

[8] G. Birkhoff and D. Carter. Rising plane bubbles. *J. Math. Mech.*, 6:769, 1957.

[9] S. Chandrasekhar. *Hydrodynamic and Hydromagnetic Stability.* Oxford University Press, Oxford, 1961.

[10] B. Cheng, J. Glimm, and D. H. Sharp. Density dependence of Rayleigh-Taylor and Richtmyer-Meshkov mixing fronts. *Phys. Lett. A*, 268:366–374, 2000.

[11] B. Cheng, J. Glimm, and D. H. Sharp. A 3-D RNG bubble merger model for Rayleigh-Taylor mixing. *Chaos*, 12:267–274, 2002.

[12] I-L. Chern, J. Glimm, O. McBryan, B. Plohr, and S. Yaniv. Front tracking for gas dynamics. *J. Comp. Phys.*, 62:83–110, 1986.

[13] A. Chorin and J. Marsden. *A Mathematical Introduction to Fluid Mechnics*. Springer Verlag, New York–Heidelberg–Berlin, 2000.

[14] J. A. Dean. *Lange's Handbook of Chemistry*. McGraw-Hill, New York, 1999.

[15] G. Dimonte and M. Schneider. Turbulent Rayleigh-Taylor instability experiments with variable acceleration. *Phys. Rev. E*, 54:3740–3743, 1996.

[16] G. Dimonte, D. L. Youngs, A. Dimits, S. Weber, M. Marinsk, S. Wunsch, C. Garsi, A. Robinson, M. Andrews, P. Ramaprabhu, A. C. Calder, B. Fryxell, J. Bielle, L. Dursi, P. MacNiece, K. Olson, P. Ricker, R. Rosner, F. Timmes, H. Tubo, Y.-N. Young, and M. Zingale. A comparative study of the turbulent Rayleigh-Taylor instability using high-resolution three-dimensional numerical simulations: The alpha-group collaboration. *Phys. Fluids*, 16:1668–1693, 2004.

[17] J. Donea, S. Giuliani, and J. P. Halleux. An arbitrary lagrangian-eulerian finite element method for transient dynamic fluid-structure interactions. *Computer Methods in Applied Mechanics and Engineering*, 33:689–723, 1982.

[18] Jian Du, Brian Fix, James Glimm, Xicheng Jia, Xiaolin Li, Yunhua Li, and Lingling Wu. A simple package for front tracking. *J. Comp. Phys.*, 2005. In press. Stony Brook University preprint SUNYSB-AMS-05-02.

[19] P. Garabedian. On steady-state bubbles generated by Taylor instability. *Proc. R. Soc. London A*, 241:423–431, 1957.

[20] E. George and J. Glimm. Self similarity of Rayleigh-Taylor mixing rates. *Phys. Fluids*, 17:054101–1–054101–13, 2005. Stony Brook University Preprint number SUNYSB-AMS-04-05.

[21] E. George, J. Glimm, J. W. Grove, X. L. Li, Y. J. Liu, Z. L. Xu, and N. Zhao. Simplification, conservation and adaptivity in the front tracking method. In T. Hou and E. Tadmor, editors, *Hyperbolic Problems: Theory, Numerics, Applications*, pages 175–184. Springer Verlag, Berlin and New York, 2003.

[22] E. George, J. Glimm, X. L. Li, Y. H. Li, and X. F. Liu. The influence of scale-breaking phenomena on turbulent mixing rates. *Phys. Rev. E*, 2005. In Press. Stony Brook University Preprint number SUNYSB-AMS-05-11.

[23] E. George, J. Glimm, X. L. Li, A. Marchese, and Z. L. Xu. A comparison of experimental, theoretical, and numerical simulation Rayleigh-Taylor mixing rates. *Proc. National Academy of Sci.*, 99:2587–2592, 2002.

[24] J. Glimm, J. W. Grove, X. L. Li, W. Oh, and D. H. Sharp. A critical analysis of Rayleigh-Taylor growth rates. *J. Comp. Phys.*, 169:652–677, 2001.

[25] J. Glimm, J. W. Grove, X.-L. Li, K.-M. Shyue, Q. Zhang, and Y. Zeng. Three dimensional front tracking. *SIAM J. Sci. Comp.*, 19:703–727, 1998.

[26] J. Glimm, J. W. Grove, X.-L. Li, and N. Zhao. Simple front tracking. In G.-Q. Chen and E. DiBenedetto, editors, *Contemporary Mathematics*, volume 238, pages 133–149. Amer. Math. Soc., Providence, RI, 1999.

[27] J. Glimm, J. W. Grove, and Y. Zhang. Interface tracking for axisymmetric flows. *SIAM J. SciComp*, 24:208–236, 2002. LANL report No. LA-UR-01-448.

[28] J. Glimm, E. Isaacson, D. Marchesin, and O. McBryan. Front tracking for hyperbolic systems. *Adv. Appl. Math.*, 2:91–119, 1981.

[29] J. Glimm, X.-L. Li, and A.-D. Lin. Nonuniform approach to terminal velocity for single mode Rayleigh-Taylor instability. *ACTA MATHEMATICAE APPLICATAE SINICA*, 18:1–8, 2002.

[30] J. Glimm, X.-L. Li, R. Menikoff, D. H. Sharp, and Q. Zhang. A numerical study of bubble interactions in Rayleigh-Taylor instability for compressible fluids. *Phys. Fluids A*, 2(11):2046–2054, 1990.

[31] J. Glimm, D. Marchesin, and O. McBryan. Stable and unstable fluid interface surfaces in petroleum engineering. Technical Report preprint, Rockefeller Univ., 1980.

[32] J. Glimm and D. H. Sharp. Stochastic partial differential equations: Selected applications in continuum physics. In R. A. Carmona and B. L. Rozovskii, editors, *Stochastic Partial Differential Equations: Six Perspectives*, Mathematical Surveys and Monographs. American Mathematical Society, Providence, 1997.

[33] J. W. Grove. Applications of front tracking to the simulation of shock refractions and unstable mixing. *J. Appl. Num. Math.*, 14:213–237, 1994.

[34] J. W. Grove and R. Menikoff. The anomalous reflection of a shock wave at a material interface. *J. Fluid Mech.*, 219:313–336, 1990.

[35] J. Hecht, U. Alon, and D. Shvarts. Potential flow models of Rayleigh-Taylor and Richtmyer-Meshkov bubble fronts. *Phys. Fluids*, 6:4019–4030, 1994.

[36] C. W. Hirt, A. A. Amsden, and J. L. Cook. An arbitrary lagrangian-eulerian computing method for all flow speeds. *J. Comp. Phys.*, 14:227–253, 1974. Reprinted in **135** (1997), pp. 203–216.

[37] D. Layzer. On the instability of superimposed fluids in a gravitational field. *Astrophys. J.*, 122:1–12, 1955.

[38] X.-L. Li. Study of three dimensional Rayleigh-Taylor instability in compressible fluids through level set method and parallel computation. *Phys. Fluids A*, 5:1904–1913, 1993.

[39] X.-L. Li, B. X. Jin, and J. Glimm. Numerical study for the three dimensional Rayleigh-Taylor instability using the TVD/AC scheme and parallel computation. *J. Comp. Phys.*, 126:343–355, 1996.

[40] P. F. Linden, D. L. Youngs, and S. B. Dalziel, editors. *Proceedings of the 4th International Workshop on the Physics of compressible turbulent mixing.* Cambridge University Press, Cambridge, England, 1993.

[41] L. G. Margolin. Introduction to "an arbitrary lagrangian-eulerian computing method for all flow speeds". *J. Comp. Phys.*, 135:198–202, 1997.

[42] R. Menikoff and C. Zemach. Rayleigh-Taylor instability and use of conformal maps for ideal fluid flow. *J. Comp. Phys.*, 51:28–64, 1983.

[43] D. Oron, L. Arazi, D. Kartoon, A. Rikanati, U. Alon, and D. Shvarts. Dimensionality dependence of the Rayleigh-Taylor and Richtmyer-Meshkov instability late-time scaling laws. *Phys. of Plasmas*, 8:2883–2890, 2001.

[44] K. I. Read. Experimental investigation of turbulent mixing by Rayleigh-Taylor instability. *Physica D*, 12:45–58, 1984.

[45] W. J. Rider and D. B. Kothe. Reconstructing volume tracking. *J. Comp. Phys.*, 141:112–152, 1997.

[46] H. F. Robey. The effect of viscosity and mass diffusion in hydrodynamically unstable plasma flows. *Phys. of Plasmas*, 11:4123–4133, 2004.

[47] D. H. Sharp. An overview of Rayleigh-Taylor instability. *Physica D*, 12:3–18, 1984.

[48] V. S. Smeeton and D. L. Youngs. Experimental investigation of turbulent mixing by Rayleigh-Taylor instability (part 3). AWE Report Number 0 35/87, 1987.

[49] D. M. Snider and M. J. Andrews. Rayleigh-Taylor and shear driven mixing with an unstable thermal stratification. *Phys. Fluids*, 6(10):3324–3334, 1994.

[50] G. I. Taylor. The instability of liquid surfaces when accelerated in a direction perpendicular to their planes I. *Proc. R Soc. London A*, 201:192–196, 1950.

[51] R. Young, J. Glimm, and B. Boston, editors. *Proceedings of the Fifth International Workshop on Compressible Turbulent Mixing.* World Scientific, Singapore, 1996. ISBN 981-02-2910-0.

[52] D. L. Youngs. Numerical simulation of turbulent mixing by Rayleigh-Taylor instability. *Physica D*, 12:32–44, 1984.

[53] Q. Zhang. The motion of single bubble or spike in Rayleigh-Taylor unstable interfaces. *Impact Comput. Sci. Engrg.*, 3:277–304, 1991.

[54] J. Zufiria. Vortex-in-cell simulation of bubble competition in Rayleigh-Taylor instability. *Phys. Fluids*, 31:440–446, 1988.